

## Static quark-antiquark interactions at nonzero temperature from lattice QCD

Dibyendu Bala,<sup>1</sup> Olaf Kaczmarek,<sup>1</sup> Rasmus Larsen,<sup>2</sup> Swagato Mukherjee,<sup>3</sup> Gaurang Parkar,<sup>2</sup> Peter Petreczky,<sup>3</sup> Alexander Rothkopf,<sup>2</sup> and Johannes Heinrich Weber<sup>4</sup>

(HotQCD Collaboration)

<sup>1</sup>*Fakultät für Physik, Universität Bielefeld, D-33615 Bielefeld, Germany*

<sup>2</sup>*Faculty of Science and Technology, University of Stavanger, NO-4036 Stavanger, Norway*

<sup>3</sup>*Physics Department, Brookhaven National Laboratory, Upton, New York 11973, USA*

<sup>4</sup>*Institut für Physik & IRIS Adlershof, Humboldt-Universität zu Berlin, D-12489 Berlin, Germany*



(Received 5 November 2021; accepted 11 February 2022; published 24 March 2022)

We study the interactions of a static quark-antiquark pair at nonzero temperature using realistic  $2 + 1$  flavor lattice QCD calculations. The study consists of two parts. The first investigates the properties of Wilson line correlators in Coulomb gauge and compares to predictions of hard-thermal loop perturbation theory. As a second step we extract the spectral functions underlying the correlators using four conceptually different methods: spectral function fits, a hard-thermal-loop-inspired fit for the correlation function, Padé rational approximation and the Bayesian reconstruction. We find that our high-statistics Euclidean lattice data are amenable to different hypotheses for the shapes of the spectral function and we compare the implications of each analysis method for the existence and properties of a well-defined ground state spectral peak.

DOI: [10.1103/PhysRevD.105.054513](https://doi.org/10.1103/PhysRevD.105.054513)

### I. INTRODUCTION

Heavy quarkonia, the bound states of a heavy quark and antiquark are a unique laboratory of the strong interactions. At the same time they constitute a central tool in the investigation of the primordial state of matter created in relativistic heavy-ion collisions: the quark-gluon plasma. In turn elucidating the properties of these strongly interacting bound states in extreme condition remains a central focus of experimental and theoretical research (see Refs. [1–4] for reviews).

Interest in heavy quarkonium in relativistic heavy-ion collisions erupted with the seminal paper by Matsui and Satz [5]. Their paper put forward two key ideas. On the one hand it argues that the formation of the deconfined medium in heavy-ion collisions will interfere with the binding of the heavy quarks through color screening and thus prevent the formation of a bound state. The second idea states that such an absence of bound states in the medium will lead to a suppression of quarkonium yields.

In heavy-ion collisions where only a few heavy quark pairs are produced, the suppression Matsui and Satz envisioned has been clearly established by experiment for both charmonium at the RHIC and bottomonium at the LHC. At increasing energies, where a wealth of heavy quarks may be produced in the initial state, it has been observed that quarkonium yields, in particular charmonium at the LHC, can be replenished. This phenomenon is attributed to recombination.

The question of whether or how color screening [and in general the interactions with a (non)thermal medium] affect the survival of heavy quarkonium states, remains an open research question. Using lattice QCD simulations it has so far been established that the free energy of a static quark-antiquark pair is indeed screened at large separations (see e.g., Ref. [6] for a recent review). The most recent lattice analysis of the static  $Q\bar{Q}$  free energy shows that the interactions are screened beyond distances larger than  $0.4/T$  [7].

Matsui and Satz took the idea of static color screening and applied it to quarkonium with finite mass constituents. In fact, their idea of melting from color screening relies on a nonrelativistic potential picture of quarkonium binding. At zero temperature such a potential picture has been highly successful in describing the phenomenology of the ground and excited states below the open heavy flavor threshold

---

*Published by the American Physical Society under the terms of the Creative Commons Attribution 4.0 International license. Further distribution of this work must maintain attribution to the author(s) and the published article's title, journal citation, and DOI. Funded by SCOAP<sup>3</sup>.*

(see e.g., Ref. [8]). The lattice calculations of quarkonium Bethe-Salpeter amplitudes at zero temperature are also consistent with the potential model [9–13].

The past two decades have seen significant progress in our understanding of heavy quarkonium systems based on the concept of effective field theory. Such a systematic approximation of QCD allows us to clarify the concept of a potential in the context of heavy (but not static) quarks. At zero temperature there exist three distinct energy scales:  $M \gg Mv \gg Mv^2$  with  $M$  being the heavy quark mass and  $v$  the relative velocity of the heavy quarks inside the bound state. By focusing on physical processes involving energies smaller than  $M$ , we may cast the description of the

quark-antiquark pair in terms of nonrelativistic Pauli spinors (pair creation at the scale  $M$  is not explicitly treated but remains present as a four-fermi interaction). This process of *integrating out* the so-called hard scale  $M$  leads to the theory of nonrelativistic QCD (NRQCD) [14], which is valid at scales up to  $Mv$ . We may further restrict our focus on e.g., the binding properties of the heavy quark-antiquark pair at the ultrasoft scale  $Mv^2$ , which leads (as long as the same degrees of freedom as in NRQCD can be identified) to a theory of color singlet  $S$  and octet  $O$  wave functions, called potential NRQCD (pNRQCD) [15]. The Lagrangian of pNRQCD has the form

$$\begin{aligned} \mathcal{L}_{\text{pNRQCD}} = & \int d^3\mathbf{r} \text{Tr} \left[ S^\dagger \left[ i\partial_0 - \left( \frac{\mathbf{D}^2}{2M} + V_S^{(0)} + \frac{V_S^{(1)}}{m_Q} + \dots \right) \right] S + O^\dagger \left[ iD_0 + \frac{\mathbf{D}^2}{2M} + V_O^{(0)} + \frac{V_O^{(1)}}{m_Q} + \dots \right] O \right] \\ & + V_A(r) \text{Tr} [O^\dagger \mathbf{r} g \mathbf{E} S + S^\dagger \mathbf{r} g \mathbf{E} O] + V_B(r) \text{Tr} [O^\dagger \mathbf{r} g \mathbf{E} O + O^\dagger O \mathbf{r} g \mathbf{E}] + \mathcal{O} \left( r^2, \frac{1}{m_Q^2} \right) + \mathcal{L}_{\text{light quarks, gluons}}. \end{aligned}$$

The singlet and octet fields depend on the label  $\mathbf{r}$  that corresponds to the distance between the heavy quark and antiquark, and the ultrasoft gluon fields depend on the center of mass coordinate,  $\mathbf{R}$  of the heavy  $Q\bar{Q}$  pair. This theory of pNRQCD puts the ideas of previous nonrelativistic potential models on a more solid footing. Its Lagrangian tells us that the propagation of color singlet and octet d.o.f. depends on two mechanisms. The first is encoded in the Schrödinger-like part of the Lagrangian (top line), in which the physics of the integrated-out gluons appears as Wilson coefficients in the form of time-independent potential terms  $V$ . Note that the static potentials  $V_{S/O}^{(0)}$  are but the first terms in a systematic expansion in powers of the inverse rest mass. In contrast to the naive potential model we see that the presence of ultrasoft gluons (on the scale  $Mv^2$ ) on the other hand introduces transitions between the singlet and octet wave functions, due to the Wilson coefficients  $V_A$  and  $V_B$ . These transitions in general cannot be summarized in terms of a simple potential and are referred to as nonpotential effects (see also the discussion in Ref. [1]). The potential picture thus describes only the lowest order (tree level) of pNRQCD. Even if we are interested in the static potential  $V_S^{(0)}$ , we therefore have to take care to distinguish between the concept of a potential (Wilson coefficient of pNRQCD) and the static energy of the quark-antiquark pair (which refers to the energy of the lowest lying excitation in its spectrum).

In some instances, depending on the specific separation of scales and a level of coarse graining in time, the terms referred to above as nonpotential terms may be absorbed into additional time-independent potential terms, allowing for a simple potential description based on a Schrödinger

equation. E.g., it has been shown that in vacuum if  $Mv^2 \ll \Lambda_{\text{QCD}}$ , the static energy and the potential agree, i.e., the static energy accessible from lattice QCD correlation functions can be used as a potential [15].

The situation at finite temperature is much more involved, as additional energy scales come into play. These are related to the thermal medium and exhibit the hierarchy  $T \gg m_D \sim gT \gg g^2T$  at weak coupling. The thermal physics may both influence the potential and nonpotential contributions to pNRQCD. In the context of pNRQCD, one may expect the medium to modify the potential, but again, this only holds true for particular scale hierarchies. E.g., when considering deeply bound quarkonium states with very small spatial extent, the real part of the potential relevant for their physics remains effectively Coulombic. In some scale hierarchies the physics of the singlet and octet transitions may be represented as additional higher-order contributions to the singlet potential, leading e.g., to the emergence of an imaginary part [16–18] related to dissipative effects in the medium.

The static in-medium potential has been studied non-perturbatively on the lattice via spectral function reconstruction and model spectral function fits. Based on the Bayesian reconstruction (BR) method [19] for spectral reconstruction the static potential has so far been investigated in quenched QCD [20,21] and in full QCD simulations based on the legacy asqtad action [22,23]. Recently the thermal potential has been obtained from APE smeared Wilson loops in the quenched approximation by means of a decomposition into parts that are symmetric and antisymmetric under  $\tau \rightarrow 1/T - \tau$ ; such a decomposition is motivated by hard thermal loop perturbation theory (HTL) [24]. These studies concluded that the real part of the potential eventually becomes screened in the deconfined phase and

have identified hints for the existence of an imaginary part once one simulates above the crossover temperature. Concurrently the potential has been extracted by fitting modified HTL spectral functions to Euclidean correlators in Ref. [25] and deploying a skewed or nonskewed Lorentzian fit in Ref. [26]. In both cases values for the real part were obtained that are significantly larger than those extracted via the direct spectral function reconstruction lying closer to the  $T = 0$  results.

Concurrent with the development of the effective field theory (EFT) approach, the past 5 years have seen rapid progress in understanding the dynamical evolution of heavy quarkonium in the context of open quantum systems (see Refs. [1,27–31] for recent reviews). In particular the role of the imaginary part of the potential has been elucidated and its relation to wave function decoherence [32,33] highlighted. It has been shown how a separation of scales in terms of energy scales is connected to a separation of time scales. Using different scale separation scenarios (and different time coarse graining prescriptions), various so-called master equations for the real-time evolution of the reduced density matrix of heavy quarkonium in a medium have been derived, revealing e.g., the subtle interplay between screening and decoherence in a hot QCD medium.

One central goal, both in the EFT and open-quantum systems community, is to go beyond the weak coupling considerations, on which many of the arguments related to scale separations are based. In order to make progress e.g., in the phenomenologically relevant temperature regime just above the QCD crossover transition, it is therefore necessary to explore whether a potential picture can be established nonperturbatively and if so, what the functional form of such a potential is.

As a starting point we therefore set out in this study to investigate the interactions of static quark-antiquark pairs at  $T > 0$  using realistic state-of-the-art lattice QCD calculations. To this end, in Sec. II we present general considerations on the real-time dynamics of static color sources and their study from Euclidean lattice simulations. The first part of our study is presented in Sec. III, where after discussing the lattice setup in Sec. III A, we investigate the lowest three cumulants of the correlation function in Sec. III B, and compare them in Sec. III C to predictions from HTL. In Sec. IV we present the investigation of the underlying spectral structure of the correlators using four different methods: spectral model fits (Sec. IV A), the HTL-motivated approach (Sec. IV B), Padé rational approximations (Sec. IV C) and the BR method (Sec. IV D). We conclude with a discussion in Sec. V.

## II. GENERAL CONSIDERATIONS

In order to connect the EFT description of quarkonium to QCD we have to carry out a matching procedure. I.e., correlation functions with the same physics content in both languages need to be identified. Demanding that their values

agree at a certain matching scale allows us to fix the Wilson coefficients of the effective theory. In the static limit  $m_Q \rightarrow \infty$ , it has been shown that the Wilson loop is the appropriate QCD quantity which we can identify with the unequal time correlation function of two color singlet fields in pNRQCD [15]. The matching condition at the leading order in the multipole expansion reads [15]

$$\begin{aligned} W_{\square}(r, t, T) &= \left\langle \exp \left[ ig \int_{\square} dz^{\mu} A_{\mu} \right] \right\rangle_{\text{QCD}} \\ &\equiv \langle S(r, 0) S^{\dagger}(r, t) \rangle_{\text{pNRQCD}}. \end{aligned} \quad (1)$$

The Wilson loop in QCD itself emerges self-consistently from the static limit of the retarded  $Q\bar{Q}$  meson correlator. By matching with different quantities related to the singlet and octet sectors, the ultimate goal here lies in identifying individually the potential ( $V_S, V_O$ ) and nonpotential contributions ( $V_A, V_B, \dots$ ) that govern the Wilson loop evolution in Minkowski time.

Let us focus on the singlet sector. Instead of studying the evolution of  $W_{\square}(r, t)$  in the real-time domain, it is advantageous to go over to its Fourier transform

$$\rho_r(\omega, T) = \int dt W_{\square}(r, t, T) e^{-i\omega t}. \quad (2)$$

This Fourier transform, as shown in Ref. [34], also coincides with the positive definite spectral function of the Wilson loop. This fact is relevant, as in Euclidean lattice simulations we do not have direct access to the real-time Wilson loop but can exploit its spectral function as a bridge between the imaginary- and real-time domains. The Euclidean Wilson loop, which we can simulate on the lattice has a spectral decomposition, housing the same spectral functions as in Eq. (2), which here is related to the lattice observable by a Laplace transform

$$W_{\square}(r, \tau, T) = \int d\omega e^{-\omega\tau} \rho_r(\omega, T). \quad (3)$$

We may thus gain insight into the real-time evolution of the Wilson loop by studying the spectral function encoded in its Euclidean counterpart. The inversion of Eq. (3) however constitutes an ill-posed inverse problem, which we will attack with four different and complementary numerical strategies in Sec. IV.

At zero temperature in a finite volume the spectral function consists of a ground state (lowest lying) delta peak separated by an energy gap from many excited state delta peaks (hybrid potential, static-light mesons etc.). In the infinite volume limit some of these excited state contributions form a continuum. The excited state contributions will be seen as deviations from a single exponential behavior of the correlator at small  $\tau$ . By performing a spectral decomposition of the nonzero temperature Euclidean time correlator in Eq. (3) in a finite volume by inserting a complete set

of energy eigenstates one can see that in addition to the ground state delta peak additional peaks in its proximity will appear. This is shown in Appendix A. The coefficients of these additional delta functions are proportional to Boltzmann factors and therefore, their relative weight will increase with increasing temperature. Thus, we will see a broadening of the zero temperature ground state peak. At finite temperature there will be some additional peaks in the  $\omega$  region corresponding to excited states, but these will not change the overall shape of the spectral function significantly, because of the already large density of states. Therefore, any possible modifications in that region should not have a significant effect on the Euclidean correlator. Thus the most interesting part of the finite temperature spectral function is the position,  $\Omega(r, T)$ , and the effective width,  $\Gamma(r, T)$ , of this dominant broadened peak. Furthermore, as also shown in Appendix A, the finite temperature spectral function could be nonzero even for  $\omega \ll \Omega(r, T)$ . We call this part of the spectral function the low energy tail. Thus we expect that the spectral function of a static  $Q\bar{Q}$  pair should consist of a ground state peak, a high energy part, which to a good approximation is temperature independent and the low energy tail.

The goal of this study is modest. Using for the first time finite temperature lattices with realistic pion masses, we set out to elucidate the lowest lying peak in the spectral function. We will refrain from making a quantitative connection of peak structures in the spectral functions to Wilson coefficients ( $V_S, V_O, V_A, V_B, \dots$ ) and solely attempt to constrain the values of  $\Omega(r, T)$  and  $\Gamma(r, T)$  as reliably as possible, given the currently available lattice data.

We also note that the overall form of the spectral function depends on the choice of our static meson operator, i.e., on the choice of the spatial part of the Wilson loop. As mentioned above, on the lattice at finite volume, the spectral function consists of a sum of delta peaks. Choosing between e.g., the Wilson loop with straight spatial lines, with deformed spatial lines, smearing the links from which to build the Wilson loop or taking instead Wilson line correlators in a particular gauge, such as Coulomb gauge, will change the amplitudes of the peaks in the spectral function but not their position. At  $T = 0$  where one encounters well separated peaks, and only their position is of interest, the tuning of operators is a common procedure to optimize the signal to noise ratio in the determination of these peak positions (see also the discussion in Refs. [35,36]). At finite temperature, where multiple peaks may congregate around a dominant central value, the changes introduced in the envelope of amplitudes by modifying the operator are less straightforward to predict. However, the position of the dominant peak and its width should be largely independent of the choice of the static meson operator. Here we may gain some intuition e.g., from HTL perturbation theory. It was shown that in the leading order of HTL perturbation theory the central position of the lowest lying spectral peak remains unaffected by the choice of either considering the Wilson

loop or the Wilson line correlator in Coulomb gauge [37]. At the same time a clear difference was found in the structures surrounding the lowest lying peak. In quenched QCD an example has been given in Ref. [1] that while the overall values of the Wilson line correlator are gauge dependent, its slope at intermediate imaginary time (thus corresponding to the position of its dominant lowest lying spectral peak) is virtually unaffected by the gauge transformation. I.e., there are indications that the properties of the lowest lying spectral structure may be extracted in an operator-independent fashion from Euclidean correlators. On the other hand the high energy part of the spectral function seems to be strongly dependent on the choice of operator. The same is true for the low energy tail of the spectral function at nonzero temperature; see Appendix A.

### III. STUDY OF THE LATTICE CORRELATION FUNCTION

#### A. Lattice setup

We performed calculations of Wilson loops and correlators of Wilson lines in Coulomb gauge at nonzero temperature in  $(2+1)$ -flavor QCD with a physical strange quark mass using gauge configurations generated by the HotQCD and TUMQCD collaborations with the Lüscher-Weisz gauge action and highly improved staggered quark action [7,38–43]. The Wilson line correlator is defined by,

$$W(r, \tau, T) = \frac{1}{3} \langle \text{Tr}(L(0, \tau)L^\dagger(r, \tau)) \rangle_T \quad (4)$$

where  $L(r, \tau) = \exp(i \int_0^\tau A_4(r, \tau') d\tau')$ . We used  $N_\sigma^3 \times N_\tau$  lattices with  $N_\tau = 10, 12$  and  $16$ , to control lattice spacing effects, and  $N_\sigma/N_\tau = 4$  [44]. Previous experience shows that the aspect ratio  $N_\sigma/N_\tau = 4$  is large enough to control finite volume effects. The light ( $u$  and  $d$ ) quark mass was set to  $m_s/20$ , which in the continuum limit corresponds to a pion mass of 161 MeV. At high temperatures,  $T > 300$  MeV we also performed calculations with a light quark mass equal to  $m_s/5$ , as quark mass effects are expected to be small in this region. The calculations performed here were part of a larger campaign by the TUMQCD Collaboration to study the interaction of static quarks at nonzero temperature and to extract the strong coupling constant [7,43]. As in the previous studies the lattice spacing has been fixed using the  $r_1$  scale defined in terms of the static  $Q\bar{Q}$  energy at zero temperature  $V(r)$  [45]

$$r^2 \frac{dV}{dr} \Big|_{r=r_1} = 1. \quad (5)$$

The values of  $r_1/a$  as well as the zero temperature Wilson loops and Wilson line correlators for  $(2+1)$ -flavor highly improved staggered quarks (HISQ) configurations have been determined in Refs. [38,40,42]. We use the parametrization

given in Ref. [42] to obtain  $a/r_1$  and the value  $r_1 = 0.3106$  fm [46]. Our calculations cover a large temperature range from as low as 120 MeV to about 2 GeV. This allows us to perform comparisons to the weak coupling calculations. The parameters of the calculations, including the temperature values, the bare gauge coupling  $\beta = 10/g^2$  and the corresponding statistics are summarized in Appendix B; an account of the zero temperature ensembles is given there as well. For Wilson loops we used 3D-HYP smeared links in the spatial direction to improve the signal. We used zero, one, two, or five steps of HYP smearings. In what follows we will use the notation  $W(r, \tau, T)$  for both Wilson line correlators and Wilson loops.

The Wilson line correlators require multiplicative renormalization. This renormalization corresponds to additive renormalization of the static  $Q\bar{Q}$  energy at zero temperature. As in our previous studies with the HISQ action we choose the renormalization scheme which corresponds to the choice  $V(r = r_0) = 0.954/r_0$ , with  $r_0$  being the Sommer scale [47]. The renormalization constants corresponding to this choice were first calculated in Refs. [38,40] for  $\beta \leq 7.825$  and later extended to larger  $\beta$  values and also refined using the result on the free energy of a static quark [7,48]. Here we use the value of the renormalization constants given in Table X of Ref. [7] for  $\beta \geq 7.15$  and in Table V of Ref. [48] for smaller  $\beta$  values.

## B. Cumulant analysis of the correlation functions

To understand the main features of our lattice results and to what extent these can constrain the spectral function of a static meson it is useful to consider the  $n$ th cumulants of the correlation functions defined as

$$m_1(r, \tau, T) = -\partial_\tau \ln W(r, \tau, T), \quad (6)$$

$$m_n = \partial_\tau m_{n-1}(r, \tau, T), n > 1. \quad (7)$$

The first cumulant  $m_1$  is nothing but the effective mass, which at nonzero lattice spacing is defined as

$$m_1(r, \tau, T) = \frac{1}{a} \ln \frac{W(r, \tau, T)}{W(r, \tau + a, T)}. \quad (8)$$

The first cumulant needs an additive renormalization which is the same as the additive renormalization of static  $Q\bar{Q}$  energy or the free energy. In what follows we will present the renormalized first cumulant using the known renormalization constants as discussed above.

Since some of the calculations in the high temperature region are performed with light quark masses significantly larger than the physical value we have to make sure that this does not affect our results. In Appendix B we compare the calculations performed at  $m_l = m_s/20$  and  $m_l = m_s/5$  and see no light quark mass dependence within statistical errors. Since we have different  $N_\tau$  values we can check the size of

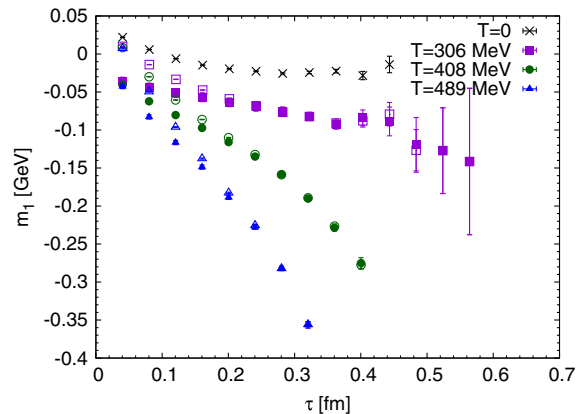


FIG. 1. The first cumulant calculated at  $r = 0.24$  fm for  $\beta = 7.825$  and  $N_\tau = 64, 16, 12$  and  $10$ , corresponding to  $T \simeq 0, 306, 408$  and  $489$  MeV, respectively. The filled symbols correspond to the subtracted correlator, while the open symbols to the unsubtracted correlator (see text).

the cutoff effects. This is also discussed in Appendix B. The size of the cutoff dependence turn out to be smaller than our statistical errors. Because of this we mostly focus our discussion on  $N_\tau = 12$  data. For this data set we have relatively small statistical errors and a sufficient number of data points in the Euclidean time direction. When appropriate we also show the  $N_\tau = 10$  and  $16$  data.

In Fig. 1 we show the first cumulant from Wilson line correlators at  $r = 0.24$  fm for  $\beta = 7.825$  and  $N_\tau = 16, 12$  and  $10$  corresponding to temperatures for  $T = 306, 408$  and  $T = 489$  MeV, respectively and compared to the zero temperature first cumulant. At  $T = 0$  the first cumulant approaches a plateau for  $\tau > 0.2$  fm. On the other hand the nonzero temperature cumulant decreases monotonically. At small  $\tau$  the difference between the zero temperature and the finite temperature first cumulant is very small and increases monotonically as  $\tau$  increases. The slope of the first cumulant increases with increasing the temperature. This means that the in-medium modifications of the spectral function are larger at larger temperatures, as expected. For the lowest temperature,  $T = 306$  MeV the decrease in the first cumulants is approximately linear in  $\tau$  around  $\tau \sim 1/(2T)$ , while for the higher temperatures this linear trend is only seen for smaller  $\tau$ , corresponding to the reduction in  $1/(2T)$ .

The small  $\tau$  behavior of the Wilson line correlators is dominated by the high omega part of the spectral function. The high  $\omega$  part of the spectral function is largely temperature independent, as discussed in the previous section, and therefore, it is not very interesting from the point of view of studying the in-medium effects on the static  $Q\bar{Q}$  pair. On the other hand it complicates the analysis and so it would be nice to get rid of it. Let us assume—following the arguments in Appendix A—that we can decompose the spectral function as  $\rho_r(\omega, T) = \rho_r^{\text{tail}}(\omega, T) + \rho_r^{\text{med}}(\omega, T) + \rho_r^{\text{high}}(\omega)$ , with  $\rho_r^{\text{med}}(\omega, T)$  containing only the spectral structures of

interest, in particular the dominant peak, and  $\rho_r^{\text{high}}(\omega)$  describing the well separated UV behavior of the spectral function. At zero temperature  $\rho_r^{\text{med}}(\omega, T)$  is a single delta function describing the ground state of a static  $Q\bar{Q}$  pair for our choice of static meson operator. Therefore, assuming that the higher lying peaks are well separated from the ground state, we may isolate it at  $T = 0$  and subtract it from  $W(r, \tau, T = 0)$ . This gives us an estimate for the contribution of the high  $\omega$  part of the spectral function. Once evaluated at zero temperature it can be used to subtract off an estimate of the high omega contribution at  $T > 0$  at the same value of  $\beta$ . We calculated the first cumulant from the subtracted correlator and the results are also shown in Fig. 1. At large  $\tau$  the subtraction has no effect; however, at small  $\tau$  the subtracted first cumulant at  $T > 0$  shows a weaker  $\tau$  dependence. At the same time it shows visible temperature dependence already for small  $\tau$ 's. At these small  $\tau$  values we see an approximately linear  $\tau$  dependence of  $m_1$  at nonzero temperature with a slope similar to the  $\tau \sim 1/(2T)$  region.

In Fig. 2 we show the subtracted first cumulants at lower temperatures for two distances,  $rT = 1/4$  and  $rT = 1/2$ . We consider the distances scaled by the temperature since with increasing temperatures the medium modification of the correlator will manifest at shorter and shorter distances. The form of  $\tau$  dependence of  $m_1$  will scale with  $rT$ . We see that for fixed  $rT$  the decrease of the first cumulant with  $\tau$  is stronger at higher temperatures. Furthermore, this decrease is larger for larger  $rT$ . We again see an approximate linear dependence of the first cumulants in  $\tau$ , except for the few largest  $\tau$  values. This feature of the first cumulants, which is a necessary consequence of the existence of the low energy tail (see Appendix A), will play an important role when modeling the spectral function of the static meson. We also point out that the behavior of the first cumulant shown in Figs. 1 and 2 is similar to the behavior of the bottomonium

first cumulants in NRQCD at nonzero temperature when extended meson operators are used [49,50].

It is interesting to compare the results of the Wilson line correlators in Coulomb gauge with the ones obtained from Wilson loops. Both types of static meson correlators have been used to obtain the static energy at zero temperature [38,40,51,52]. The first cumulants for Wilson line correlators and from smeared or unsmeared Wilson loops have been compared in Ref. [43] for zero temperature. It turned out that both approach the same plateau value for sufficiently large  $\tau$ . At small  $\tau$  the first cumulants for Wilson loops are systematically larger than those for the Wilson line correlators. The first cumulants for the Wilson line correlators approach the plateau at smaller Euclidean time separation and have smaller errors [43]. In this sense the Wilson line correlators in Coulomb gauge are very good in projecting to the ground state, while there are significant excited state contributions in the Wilson loops. We performed a similar comparison of Wilson line correlators in Coulomb gauge and Wilson loops with different levels of HYP smearings for  $T = 411$  MeV ( $\beta = 7.825$ ) and  $N_\tau = 12$ . As in the zero temperature case there is a significant difference in the first cumulants for Wilson loops and Wilson line correlators at small Euclidean time as in the zero temperature case due to the excited state contamination, or equivalently due to  $\rho_r^{\text{high}}(\omega)$ . Therefore, in Fig. 3 we show the comparison of the Wilson loops and Wilson line correlators in Coulomb gauge at two distances,  $rT = 1/4$  and  $rT = 1/2$ , in terms of the subtracted first cumulants. At the smaller distance the first cumulant from Wilson line correlators and for Wilson loops with different levels of HYP smearing agree within errors. For the larger distance,  $rT = 1/2$  the two correlators agree at small  $\tau$ , where we see a nearly linear decrease of the first cumulants, while at large  $\tau$ , the nonlinear behavior in  $\tau$  of the first cumulants depends on the number of HYP smearings, and is also different for the Wilson line correlator in Coulomb gauge. Thus the large Euclidean time behavior

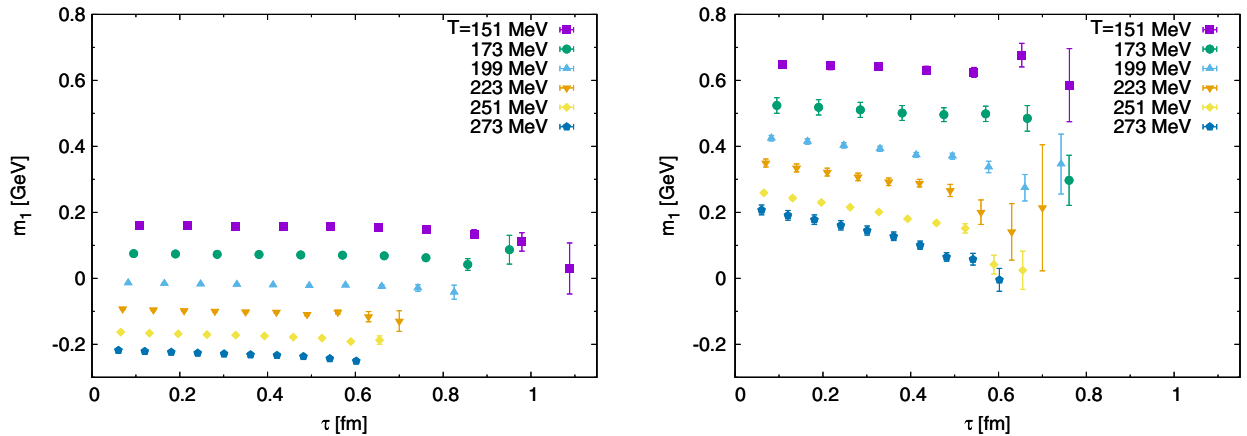


FIG. 2. The first cumulant as a function of  $\tau$  obtained on  $N_\tau = 12$  lattices for  $rT = 1/4$  (left) and  $rT = 1/2$  (right) at different temperatures.

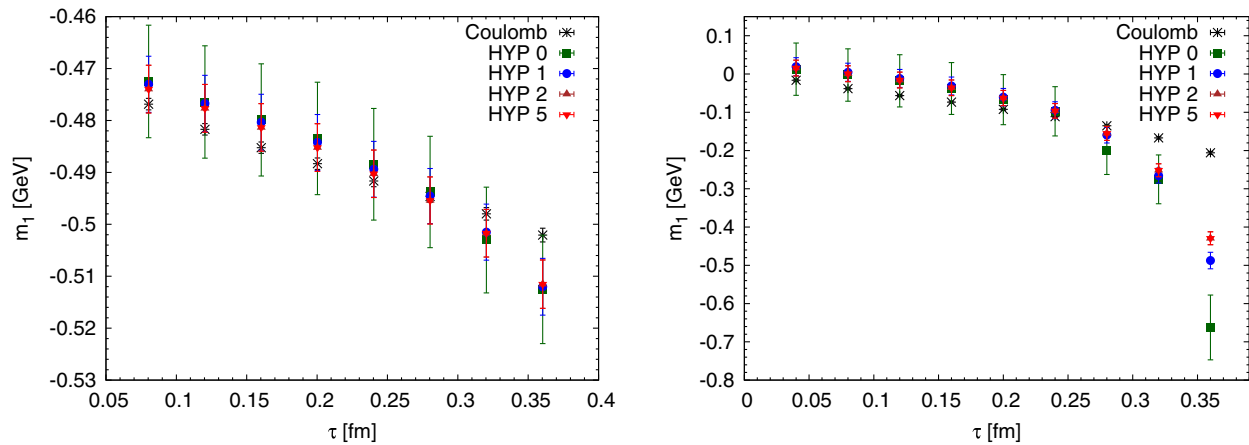


FIG. 3. Comparison of the subtracted first cumulant from the Wilson line correlators in Coulomb gauge and smeared Wilson loops with different levels of HYP smearing at  $T = 408$  MeV with  $N_\tau = 12$  and  $\beta = 7.825$ . The left panel shows the results for  $rT = 1/4$ , while the right panel shows the result for  $rT = 1/2$ .

depends on the choice of the static meson operator. This is to be expected as explained above. The situation is similar to the case of the bottomonium correlator in NRQCD at nonzero temperature when different extended meson operators are used [49,50]. Since the behavior of the first cumulant at  $\tau$  close to  $1/T$  depends on the choice of the static meson operators it is nontrivial to obtain physical information from  $W(r, \tau, T)$  in this  $\tau$  region.

In order to better understand our numerical results on the first cumulants and see to what extent these can constrain the spectral function of a static meson it is helpful to calculate higher cumulants of the correlator. In the following we consider the cumulants of the subtracted correlator as we are interested in exploring the  $\tau$  dependence caused by thermal broadening of the dominant peak. To evaluate higher cumulants we performed fits of the first cumulants of the subtracted correlator using fourth order polynomials, and estimated the higher cumulants by taking the derivatives of the resulting polynomial. The results for the second cumulants for three distances,  $rT = 1/4, 1/2$  and  $1$  at several temperatures are shown in Fig. 4 for  $N_\tau = 12$ . The errors on the cumulants have been estimated using the

jackknife procedure. Since the second cumulant is negative, and the square root of the negative second cumulant may be related to the width, as discussed later, in the figure we show  $\sqrt{-m_2}$  in temperature units. We see that the errors on the second cumulants increase with decreasing temperature. At short distances, the second cumulant is approximately constant for small  $\tau$  and then starts to increase rapidly with increasing  $\tau$ . For  $rT = 1$  the almost constant behavior of  $m_2$  is only seen for the highest two temperatures. The results for  $T < 251$  MeV are not shown as these have much larger errors. However, within these large errors the second cumulant is compatible with a constant at these temperatures.

In Fig. 5 we show the third cumulant of the Wilson line correlator, obtained from a fourth order polynomial fit to the first cumulant  $m_1$ , as a function of  $\tau T$  in temperature units. The results are shown for three representative distances,  $rT = 1/4$ ,  $rT = 1/2$  and  $rT = 1$ . We only show our findings for the third cumulant for  $T \geq 334$  MeV as at lower temperatures the errors are too large to extract meaningful information from them. Furthermore, for  $rT = 1/4$  the errors are already very large for  $T = 334$  MeV. The

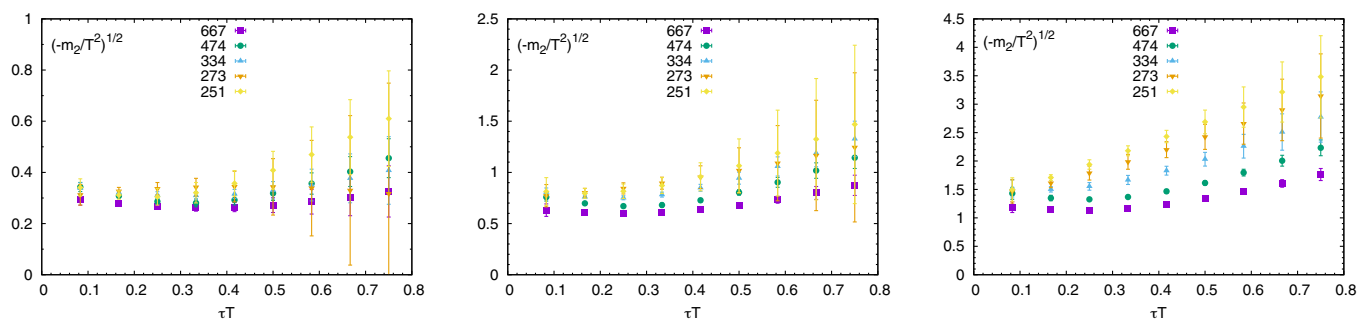


FIG. 4. The second cumulants  $m_2$ , obtained from a fourth order polynomial fit to the first cumulant  $m_1$ , of the subtracted static meson correlator on  $N_\tau = 12$  lattices for  $rT = 1/4$  (left),  $rT = 1/2$  (middle) and  $rT = 1$  (right) for several temperatures. The different symbols correspond to different temperatures given in MeV.

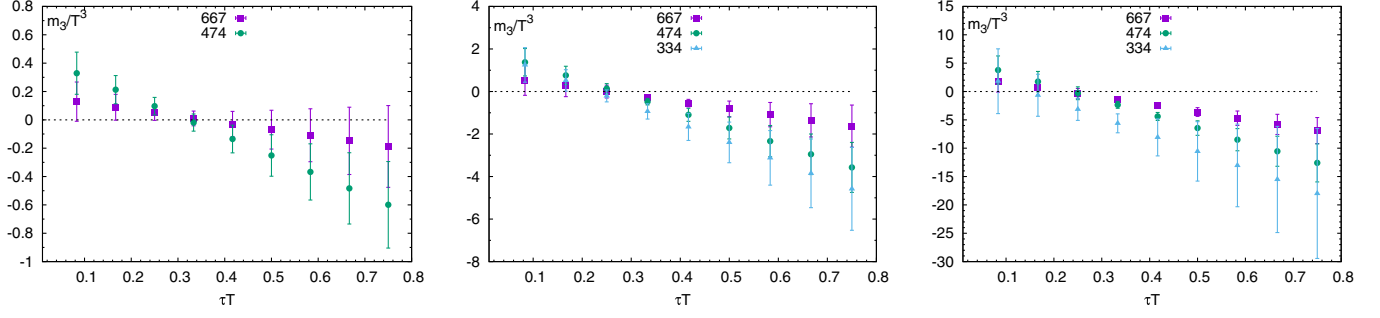


FIG. 5. The third cumulants  $m_3$ , obtained from a fourth order polynomial fit to the first cumulant  $m_1$ , of the subtracted static meson correlator on  $N_\tau = 12$  lattices for  $rT = 1/4$  (left),  $rT = 1/2$  (middle) and  $rT = 1$  (right) for several temperatures. The different symbols correspond to different temperatures given in MeV.

absolute value of the third cumulant increases rapidly with increasing  $rT$  and decreases with increasing temperature. These features can already be deduced by looking at the result for the second cumulant. For  $\tau T > 0.35$  the third cumulant is negative, while for  $\tau < 0.3$  it is positive but small given the errors. The small positive third cumulant at small  $\tau$  is equivalent to having a nearly constant second cumulant.

From Fig. 5 it is clear that estimating the fourth and higher order cumulants from the present lattice results is very challenging. This will be important when considering the parametrization of the spectral function of a static meson, as the data can only constrain such a limited amount of parameters. Hence any such parametrization should not contain more than three or four parameters.

### C. Comparison to HTL predictions

At high temperatures, it is expected that the Wilson loops and the Wilson line correlators in Coulomb gauge can be described in the weak coupling approach. The Wilson loops and Wilson line correlators have been calculated at leading order in HTL [16,37]. The HTL approximation is valid when  $r \sim 1/m_D$  [17], with  $m_D$  being the leading order Debye mass in QCD. At distances  $r \ll 1/m_D$  this approximation is not expected to work. In the HTL approximation the logarithm of the Wilson loop or the Wilson line correlator can be written as

$$\begin{aligned} \log W(r, \tau, T) = & -\text{Re}V(r, T) \times \tau \\ & + \int_{-\infty}^{\infty} \frac{d\omega}{2\pi} (e^{-\omega\tau} + e^{-\omega(\beta-\tau)}) \\ & \times (1 + n_B(\omega)) \sigma_r(\omega, T) + \text{const}, \end{aligned} \quad (9)$$

where  $n_B(\omega) = (\exp(\omega/T) - 1)^{-1}$ . The spectral function  $\sigma_r(\omega, T)$  is related to the HTL spectral functions of the transverse and longitudinal gluons and is distinct from the spectral function  $\rho_r(\omega, T)$ . For the Wilson line correlator, it only depends on the spectral function of the longitudinal gluons.

The important feature of this correlator is that the static energy exists,

$$\begin{aligned} E_s^{\text{HTL}}(r, T) = & \lim_{t \rightarrow \infty} i \frac{\partial \log W(r, \tau = it, T)}{\partial t} \\ = & \text{Re}V(r, T) - i \text{Im}V(r, T). \end{aligned} \quad (10)$$

At leading order, the real or imaginary parts are given as

$$\begin{aligned} \text{Re}V(r, T) = & -\frac{g^2 C_F}{4\pi} \left( \frac{e^{-m_D r}}{r} + m_D \right) \\ \text{Im}V(r, T) = & \frac{g^2 C_F}{4\pi} T \int_0^\infty dz \frac{2z}{(z^2 + 1)^2} \left[ 1 - \frac{\sin z m_D r}{z m_D r} \right]. \end{aligned} \quad (11)$$

The real part of the potential  $\text{Re}V(r, T)$ , in this approximation, is at leading order identical to the singlet free energy in Coulomb gauge [16,17]. We observe the  $\tau$  dependence in the above correlator consists of linear and periodic part in  $\tau$ . This particular  $\tau$  dependence of the HTL correlator along with the fact that  $\sigma_r(\omega, T)$  has a  $1/\omega$  singularity allows us to have a well-defined limit in Eq. (10). In Sec. IV B, while calculating the static energy nonperturbatively we will parametrize the correlator as a combination of linear and periodic parts in  $\tau$ . The obvious consequence of a parametrization as in Eq. (9) is that the first cumulant of  $W(r, \tau, T)$  is antisymmetric around the midpoint  $\tau = 1/(2T)$ .

Since we study the Wilson line correlators in a large temperature range, including high-temperature values it makes sense to compare the lattice results with the weak-coupling ones. Comparison with the HTL perturbative result is also important since it gives some insight into the general features of the spectral function and how these features manifest in the cumulants of the Euclidean time correlator. Therefore, in Fig. 6 we show the spectral functions corresponding to Wilson line correlators for different  $r$  at  $T = 667$  MeV in the HTL approximation. Note that we use a different renormalization prescription compared to Ref. [37] as well as the two-loop running of the coupling constant with  $\Lambda_{\overline{\text{MS}}}^{n_f=3} = 332$  MeV [53]. We will use this choice for the gauge coupling throughout this paper. We see a peak in the spectral function at  $\omega = \text{Re}V(r, T) = F_S(r, T)$ , which can

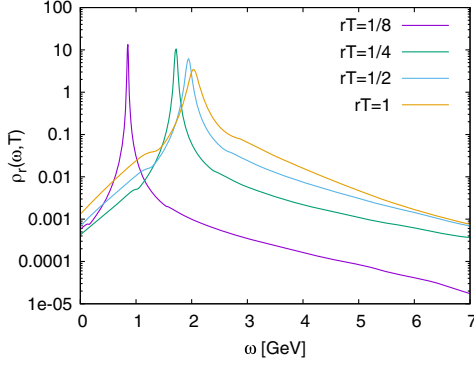


FIG. 6. The HTL spectral function for  $T = 667$  MeV for different  $r$ .

be well described by a skewed Lorentzian for frequencies around the location of the peak [37]. Far away from the peak position, the spectral function is described by different structures, distinct from the Lorentzian.

In general, one has to expect that the nonperturbative spectral function such as the one calculated on a lattice contains further structures. In particular, the lattice spectral function has a large UV continuum part along with a tail at very low  $\omega$ . The HTL feature of the lattice spectral functions could only come from the medium dominated part of the spectral function ( $\rho_r^{\text{med}}(\omega, T)$ ). Therefore, we could possibly see the HTL-like features in the nonperturbative correlator near the  $\tau \sim 1/(2T)$  region if these are sufficiently separated from any further structures.

We consider the comparison between the lattice and HTL result for the Wilson line correlator in terms of its first cumulant,  $m_1$ . The first cumulant should be sensitive to the peak position of the spectral functions. In the absence of a peak width, i.e., when  $\rho_r^{\text{med}}(\omega, T) \sim \delta(\omega - E_0(r))$ ,  $m_1$  should approach the energy of a static  $Q\bar{Q}$  pair  $E_0$  at intermediate  $\tau$ . It is known that the leading order perturbative result does not provide an accurate description of the static  $Q\bar{Q}$  energy at zero temperature.

For this reason, we naturally expect that at finite temperature nonperturbative real and imaginary parts of the complex static energy defined through the parametrization of Eq. (9) will be different from the expressions given in Eq. (11). Therefore, a nonperturbative investigation of this complex static energy is very important, which we will discuss in detail in Sec. IV B.

Furthermore, the static energy needs to be renormalized, and the renormalization condition used on the lattice is different from the one in the  $\overline{\text{MS}}$  scheme. Connecting these two renormalization schemes is a nontrivial task. We also know that the real part of the static energy is given by the so-called singlet  $Q\bar{Q}$  free energy,  $F_S(r, T)$  in the HTL approximation [17], as discussed above. Therefore, when comparing the lattice results on  $m_1$  to the HTL results we will assume that the peak position is similar to  $F_S(r, T)$  and subtract the latter from the first cumulant.

As mentioned above the HTL calculation is not expected to describe the spectral function at large  $\omega$ . Therefore, we should use the subtracted first cumulant when comparing the lattice and HTL results, or simply ignore the data points at small  $\tau$  in the comparison. But the HTL feature in the correlator could only appear in the data points around  $\tau \sim 1/2T$ , where the effect of this subtraction is small.

We performed a comparison of the lattice results on the subtracted first cumulant with leading-order HTL calculations for  $T = 474$  MeV and  $T = 667$  MeV. In the HTL calculations we used three values of the renormalization scale  $\mu = \pi T, 2\pi T$  and  $4\pi T$ . The comparison is shown in Fig. 7 for  $T = 667$  MeV and four representative distances  $rT = 1/4, 1/2, 3/4$  and 1. The lattice and the HTL results for  $m_1$  share some qualitative features, namely they decrease monotonically with increasing  $\tau$ . This decrease of  $m_1$  with  $\tau$  around  $\beta/2$  comes from the fact that the spectral function is not a delta function but rather a broad peak (see Fig. 6) and the slope of  $m_1$  is loosely related to the width of the peak.

The HTL curve is antisymmetric with respect to  $1/(2T)$  over the whole  $\tau$  range, while the lattice data do not show the same antisymmetry. This is expected as the lattice correlator gets contributions from both  $\rho_r^{\text{high}}(\omega, T)$  and  $\rho_r^{\text{tail}}(\omega, T)$ . However, as we will see in Sec. IV B, non-perturbative data are compatible with a small antisymmetric region around  $\tau \sim 1/(2T)$ .

We mentioned earlier that the leading-order HTL results for the real part of the static energy and the singlet free energy agree exactly; hence, the corresponding  $m_1 - F_S$  vanishes at  $\tau = 1/(2T)$ . However, the lattice result for  $m_1 - F_S$  is nonzero at  $\tau = 1/(2T)$ . This implies that the real part of the static energy that will be determined in Sec. IV B must be different from the singlet free energy. The slope of  $m_1$  around  $\tau \sim 1/(2T)$  is much larger for the lattice correlator than for the leading-order HTL curve. This corresponds to the fact that the nonperturbative imaginary part determined from the lattice data in Sec. IV B is significantly different from the expression given in Eq. (11).

The comparison turned out to be similar for  $T = 474$  MeV. We also performed a comparison between the lattice and HTL calculations at the highest temperature available,  $T = 1938$  MeV. Since we do not have the corresponding zero temperature result, here the comparison is performed in terms of the unsubtracted cumulants. We see that also at the highest temperature the lattice data differs from the perturbative HTL data. The first cumulant calculated on the lattice has a steeper  $\tau T$  dependence than the perturbative HTL result even at this very high temperature, see Fig. 8. This indicates that the imaginary part of the nonperturbative result is much larger than the counterpart in the perturbative calculation.

In Fig. 9 we show the comparison of the lattice and HTL results for the second cumulant,  $m_2$  for  $T = 667$  MeV and three representative distances,  $rT = 1/4, 1/2$  and 1. We

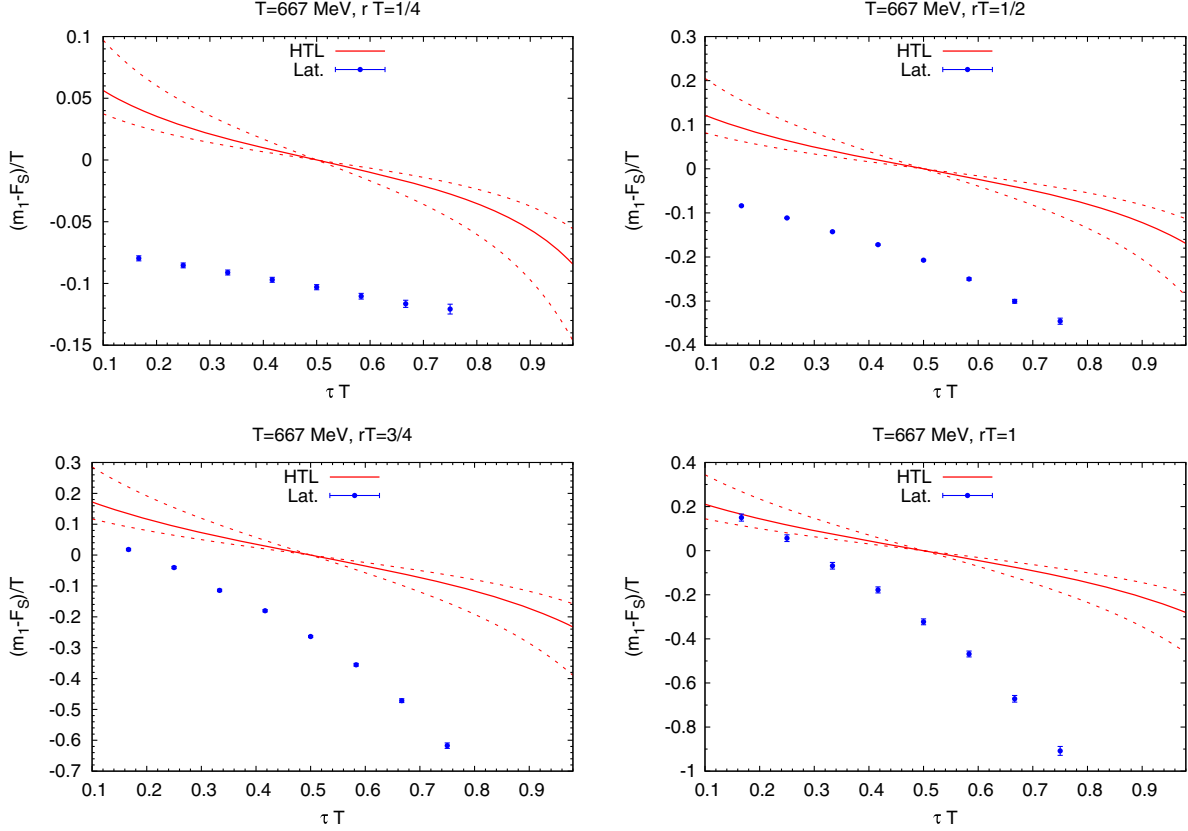


FIG. 7. The comparison of  $m_1 - F_S$  on the lattice (subtracted) with HTL results at  $T = 667$  MeV for  $rT = 1/4, 1/2, 3/4$  and 1. The HTL result for  $\mu = 2\pi T$  are shown as solid lines. The dashed lines correspond to a variation of the scale  $\mu$  by a factor of 2.

choose the renormalization scale in the HTL calculation to be  $\mu = 2\pi T$  and vary it by a factor of 2 around this value. Unsurprisingly, there is no quantitative agreement between the lattice results and leading-order HTL as already visible from Fig. 7. The fact that  $m_2$  on the lattice is constant at small  $\tau$  is due to the subtraction of the UV contribution, while the fact that  $m_2$  is not a constant at large  $\tau$  is due to the low-energy tail. Since neither of these are present in the leading-order HTL result, the mismatch between lattice and leading-order HTL is particularly pronounced in these regions.

#### IV. STUDY OF THE SPECTRAL FUNCTION AND ITS GROUND STATE PEAK

We will in the subsections of this section make four different attempts to analyze the lattice results. The four methods are: fit with a finite width spectral function (Sec. IV A), fit with the HTL ansatz (Sec. IV B), a Padé fit (Sec. IV C), and a fit using Bayesian methods (Sec. IV D). We will outline here the basic idea behind each method and the pros and cons of each choice, and leave a more technical description for each subsection. We clearly state that the first three approaches (Bayesian methods are an exception) only aim at identifying and parametrizing the lowest, dominant spectral feature. Thus, the inability of

their results to reproduce the input data over the complete  $\tau$  range has to be expected. We stress that this is nothing unusual: the same applies to almost any analysis of zero-temperature lattice correlators that may have to leave out the first few time steps due to not having enough independent information in this range to fully constrain the complex UV structure affecting those data. The aim is to leave it to the reader to judge each method based on the results put forth in this paper and let them decide which one they prefer.

The first method used in Sec. IV A is a simple fit, using a model spectral function with a well defined position and width. This choice comes from the observation that when one uses zero temperature results to remove contributions coming from higher energy excitations, the first cumulant takes a form that is well approximated by a low order polynomial, sometimes even that of a straight line. The benefit of this method is that it gives a precise answer to the question “What is the position and width of the dominant feature in the spectral function?” with a fit that works very well, excluding the first and last point. The downside is that for it to work, the high energy contributions to the correlator have to be removed using zero temperature results, a procedure which might not be well defined. Also the actual shape of the dominant spectral feature is not determined, but rather only its position and effective width.

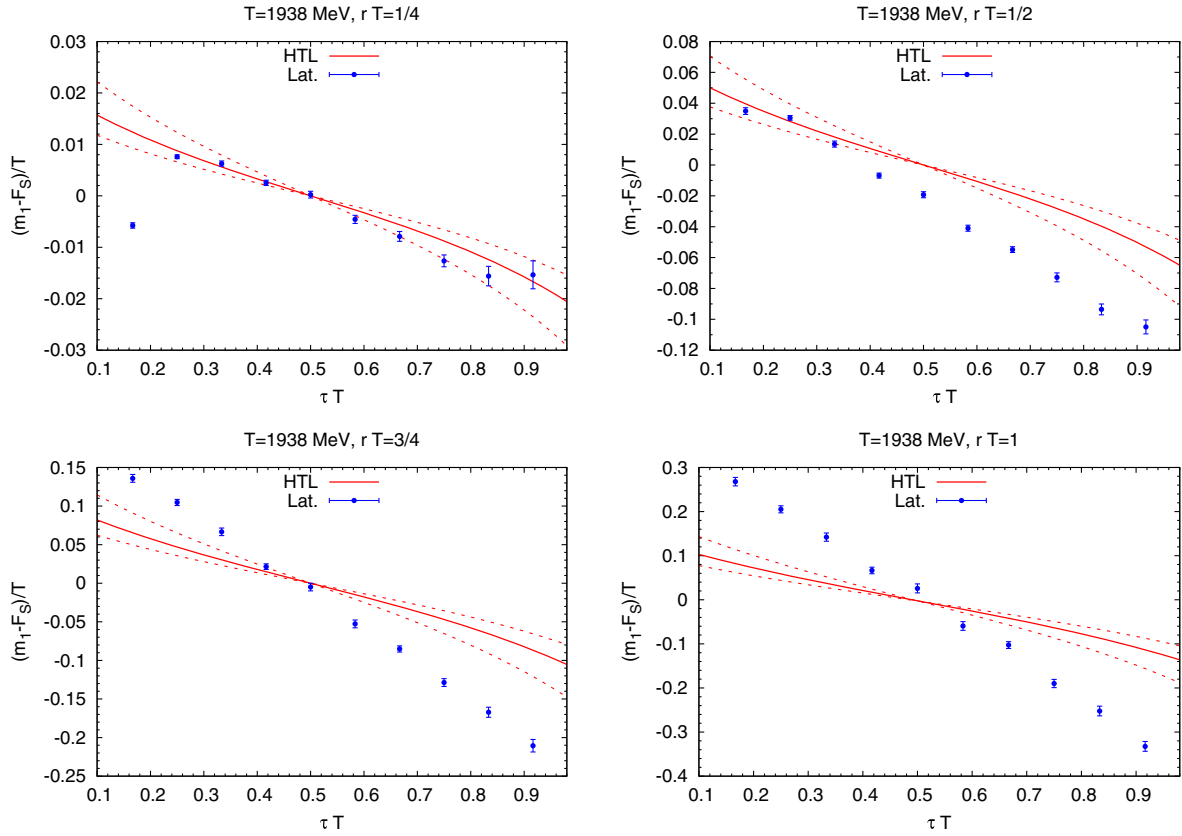


FIG. 8. The comparison of  $m_1 - F_S$  calculated on the lattice with HTL results at  $T = 1938$  MeV for  $rT = 1/4, 1/2, 3/4$  and 1. The HTL results for  $\mu = 2\pi T$  are shown as solid lines. The dashed lines correspond to a variation of the scale  $\mu$  by a factor of 2.

The second method is in Sec. IV B and uses an ansatz motivated by HTL to fit in a narrow range around  $\tau \sim 1/(2T)$  to extract physically relevant information. Namely, one parametrizes the  $\tau$  dependence around  $1/(2T)$  exactly like the  $\tau$  dependence in Eq. (9). In this method the peak position and peak width can be interpreted as a real and imaginary part of the thermal static energy. As shown earlier in this paper, HTL cannot explain the full spectral function. The HTL-motivated fit only attempts to describe the dominant feature

of the spectral function which is responsible for the thermal static energy.

The third method used in Sec. IV C is the Padé interpolation. This approach operates on the Fourier transformed lattice data, instead of directly on the correlator. The rational interpolation of the Matsubara frequency correlator is subsequently rotated to real time. In our mock data tests, this method has shown to give reasonable results for the position of the peaks, but failed to reliably estimate the

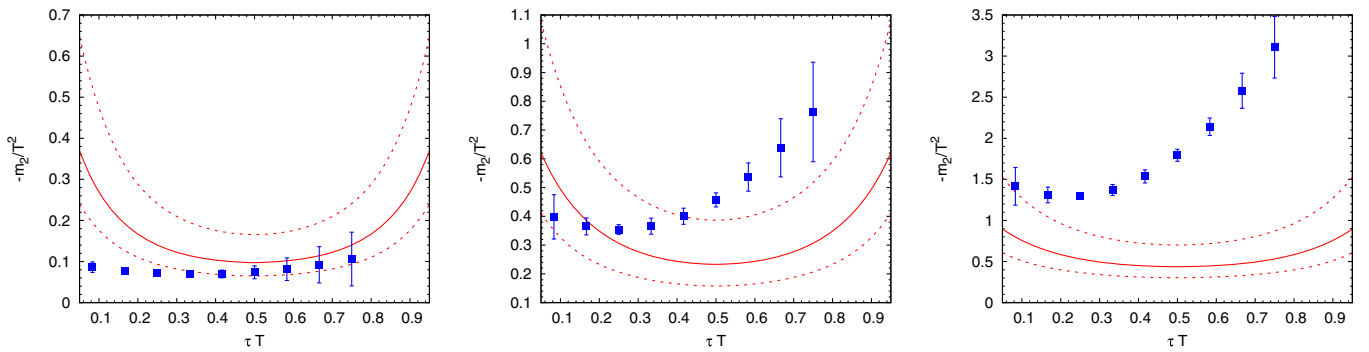


FIG. 9. The second cumulant, obtained from a fourth order polynomial fit to the first cumulant  $m_1$ , of the subtracted Wilson line correlators as function of  $\tau$  at  $T = 667$  MeV calculated on  $N_\tau = 12$  lattices and in HTL perturbation theory (lines) for  $rT = 1/4$  (left),  $rT = 1/2$  (middle) and  $rT = 1$  (right). The solid line corresponds to the choice of the renormalization scale  $\mu = 2\pi T$ , while the dashed lines correspond to the scale choice  $\mu = \pi T$  and  $4\pi T$ .

width of the spectral function. By construction the Padé approach does not need to reproduce the input data and we find that the reconstructed spectral function indeed does not fulfill the original spectral decomposition. The method requires a high quality of the input data, as it does not contain a regulator of the statistical noise.

The fourth and last method we use is the Bayesian reconstruction method described in Sec. IV D, which is based on Bayesian inference. The basic idea here is to regularize a  $\chi^2$  fit with an additional functional, which encodes how compatible the fitted spectral function is with prior knowledge one possesses on the spectrum, such as its positivity. This method is constructed such that it will always reproduce the Euclidean input data points within their statistical uncertainty. It has shown to outperform the maximum entropy method in the reproduction of sharp peaked features but may suffer from ringing artifacts in the reconstruction of extended spectral features, and requires high precision data. However, it was realized that correlators on the finer lattices with an improved gauge action contain non-negligible contributions with negative weights that render the BR method inapplicable.

### A. Determination of the ground state peak from spectral function model fits

In order to constrain the spectral function  $\rho_r(\omega, T)$  from limited data on Euclidean time correlation functions we need to assume some functional form for it. As for the analysis of the cumulants we assume that the spectral function can be written  $\rho_r(\omega, T) = \rho_r^{\text{tail}}(\omega, T) + \rho_r^{\text{med}}(\omega, T) + \rho_r^{\text{high}}(\omega)$ , where  $\rho_r^{\text{high}}(\omega)$  is assumed to be the temperature independent high frequency part of the spectral function and  $\rho_r^{\text{med}}(\omega, T)$  contains the dominant peak structure. Based on general grounds and EFT arguments it is natural to assume that  $\rho_r^{\text{med}}(\omega, T)$  has a Lorentzian form. However, for a Lorentzian form the integral in Eq. (3) will not converge at the lower integration limit. We also do not expect that the Lorentzian form can describe the spectral function well below  $\omega = \Omega(r, T)$ . This follows from the general properties of the spectral function discussed in Appendix A. In the case of the HTL spectral function we have seen that while around the peak the spectral function appears to be Lorentzian, different structures dominate the spectral function far away from the peak, in particular at very low frequency; see Fig. 6. Thus in addition to the parametrization of the peak of the spectral function, we also need to parametrize the behavior of the spectral function at very low frequency, i.e., the low energy tail. This part of the spectral function will affect the correlation function at large values of  $\tau$ . Unfortunately, we do not have a well motivated form for this part of the spectral function. Furthermore, for calculations in finite volume the spectral function is not a continuous function but a discrete sum of delta functions with an envelope function of certain shape. For small

volumes as used in the present calculations there could be significant distortion of the envelope function, since the number of low lying energy levels and the corresponding number of  $\delta$  peaks is quite limited. This is especially the case for the low  $\omega$  tail as it extends over a large  $\omega$  range below the dominant peak position, including negative  $\omega$  values.

The information we have on the different structures in the spectral function is also quite limited. At small  $\tau$  values only the first two cumulants can be determined with the third cumulant being zero within the estimated errors. Therefore, at small  $\tau$  the lattice data are only sensitive to the position and the effective width of the dominant peak, and a Gaussian form provides a simple parametrization for this that avoids the convergence problem in Eq. (3). At larger  $\tau$  the correlation function is sensitive to the low energy tail, i.e., the region  $\omega \ll \Omega(r, T)$ . In the previous section we have seen that in this region the third cumulant is also nonzero, but cumulants beyond the third one cannot be constrained by our lattice data. While it would be tempting to parametrize the low  $\omega$  tail of the spectral function by a series of delta functions avoiding any bias, in practice it is impossible to constrain all the corresponding parameters. We need to approximate this part of the spectral function by a single delta function. Thus a simple parametrization of the Wilson line correlator function consistent with the above observations is the following:

$$W(r, \tau, T) = A_P(r, T) \exp(-\Omega(r, T)\tau + \Gamma_G(r, T)^2 \tau^2 / 2) + A_{\text{cut}}(r, T) \exp(-\omega_{\text{cut}}(r, T)\tau), \quad (12)$$

with  $A_{\text{cut}} \ll A_P$  and  $\omega_{\text{cut}} \ll \Omega$ . The first cumulant corresponding to this form will decrease linearly at small  $\tau$ , while exhibiting a nonlinear behavior for large  $\tau$  as observed in our lattice results. We performed correlated fits of our lattice data using Eq. (12) and determined the parameters  $A_P, \Omega, \Gamma_G, A_{\text{cut}}$  and  $\omega_{\text{cut}}$ . The fits describe the lattice data very well, with the possible exception of the data at the smallest  $\tau$  value. The details of these fits are discussed in Appendix C.

The peak position,  $\Omega(r, T)$  is shown in Fig. 10 as a function of the distance  $r$  for different temperatures. It shows no temperature dependence and agrees with the zero temperature static energy. The fact that  $\Omega$  is close to the zero temperature static energy can be easily understood from Fig. 1. The subtracted first cumulant at smallest  $\tau$  is already close to the zero temperature plateau and shows linear behavior at small  $\tau$ . A linear extrapolation naturally gives the zero temperature static energy. The width of the dominant peak depends on the specific parametrization of the spectral function and the Gaussian form has no physical motivation. A parametrization independent definition of the effective width could be the width at the half maximum. For a Gaussian form this means  $\Gamma = \Gamma_G \sqrt{2 \ln 2}$ . In Fig. 10 we also show the effective width  $\Gamma$  as a function of the distance,  $r$  at different temperatures. We see that  $\Gamma$  increases with

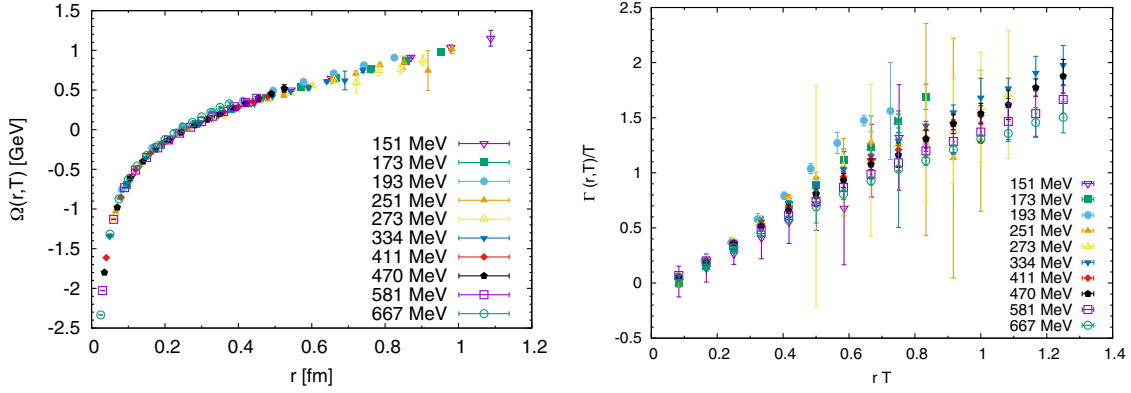


FIG. 10. The peak position of the spectral function (left) and the width (right) as functions of the separation  $r$  obtained from Gaussian fits of the  $N_\tau = 12$  data.

increasing  $r$ . We also see that when plotted as a function of  $rT$  the effective width in temperature units shows very little temperature dependence. This is expected at very high temperature, but not in the temperature range studied by us. For the other two fit parameters we find that  $\omega_{\text{cut}} \ll \Omega$  and  $A_{\text{cut}} \ll A_p$  in accordance with our expectations. The same parametrization of the spectral function has been used in the analysis of NRQCD bottomonium correlators at nonzero temperature [49,50]. It has been observed that different bottomonium states have thermal width, but no significant mass shift has been observed. Furthermore, the thermal width turned out to be larger for higher lying bottomonium states that have larger size [49,50]. Thus the thermal modification of static  $Q\bar{Q}$  states and bottomonium is quite similar. Furthermore, the bottomonium Bethe-Salpeter amplitudes also do not show large temperature modifications [13]. Using this result a potential model analysis resulted in a potential that has a real part which is identical to the zero temperature static energy [54].

### B. Determination of the ground state peak via the HTL-motivated method

In this section, we will use the method of Ref. [24] to obtain the position and the width of the dominant peak of the static  $Q\bar{Q}$  spectral function. In this method, the peak position  $\Omega(r, T)$  and peak width  $\Gamma(r, T)$  of the dominant peak are interpreted as the real and imaginary parts of the thermal static energy  $E_s(r, T)$ . Quantitatively, one assumes the following limit exists:

$$E_s(r, T) = \lim_{t \rightarrow \infty} i \frac{\partial \log W(r, t, T)}{\partial t} = \Omega(r, T) - i\Gamma(r, T). \quad (13)$$

Here,  $W(r, t, T)$  is the real-time correlator obtained as the Fourier transform of the spectral function  $\rho_r(r, \omega)$ .

Below the crossover temperature  $W(r, \tau, T=0) \sim \exp(-\Omega\tau)$  for  $0 \ll \tau \ll 1/T$  follows from a transfer matrix argument, and therefore the above limit exists trivially. However, above the crossover temperature, the existence

of the limit in Eq. (13) is a nontrivial statement whose consequences are important for various applications like in open quantum systems [32] or the construction of a vector current spectral function [55].

The definition of the static energy involves a  $Q\bar{Q}$  correlator, whose large-time behavior is governed by the lowest, dominant feature of  $\rho_r^{\text{med}}(\omega, T)$ . As a consequence, it is sufficient to determine the structure of the dominant peak of the spectral function to obtain the thermal static energy. In this HTL-motivated method, we model the dominant peak of the spectral function such that the above limit exists.

In Sec. III C we mentioned that for the leading-order HTL correlator the limit in Eq. (13) exists. We observed that this is possible because the correlator can be written as a combination of a part linear in  $\tau$  and a part periodic in  $\tau$ , cf. Eq. (9). Now let us see whether the nonperturbative data near  $\tau \sim 1/(2T)$  could be parametrized by a combination of periodic and linear parts in  $\tau$ . Motivated by this we write the following parametrization of the  $Q\bar{Q}$  correlator near  $\tau \sim 1/(2T)$ :

$$\begin{aligned} \log W(r, \tau, T) = & -\Omega(r, T)\tau \\ & + \int_{-\infty}^{\infty} d\omega \Sigma_r(\omega, T) (e^{-\omega\tau} + e^{-\omega(\beta-\tau)}) \\ & + \text{const.} \end{aligned} \quad (14)$$

The condition for the limit in Eq. (13) is then

$$\lim_{t \rightarrow \infty} \int_{-\infty}^{\infty} d\omega \Sigma_r(\omega) \omega (e^{-i\omega t} - e^{-\omega(\beta-it)}) = \text{const.} \quad (15)$$

Using the fact that  $\lim_{t \rightarrow \infty} (e^{-i\omega t} - e^{-\omega(\beta-it)}) = -2\pi i \omega \delta(\omega)$ , we observe that the above limit will exist only if  $\Sigma_r(\omega) \sim \frac{1}{\omega^2}$  as  $\omega \rightarrow 0$ .

Without loss of generality we can introduce a factor  $(1 + n_b(\omega))$  and write

$$\Sigma_r(\omega, T) = (1 + n_b(\omega))\eta_r(\omega, T). \quad (16)$$

Since the function  $(1 + n_b(\omega))$  already contains a factor of  $1/\omega$ , the  $\eta_r(\omega, T)$  should also contain  $1/\omega$  at small  $\omega$ . Then Eq. (14) becomes,

$$\begin{aligned} \log W(r, \tau, T) &= -\Omega(r, T)\tau \\ &+ \int_{-\infty}^{\infty} d\omega \eta_r(\omega, T) \frac{\exp(\omega\tau) + \exp(\omega(\beta - \tau))}{\exp(\omega\beta) - 1} \\ &+ \text{const.} \end{aligned} \quad (17)$$

$\eta_r(\omega, T)$  can only be an odd function  $\omega$ . The most general expansion of the function  $\eta_r(\omega, T)$  consistent with the existence of thermal static energy can then be written as

$$\eta_r(\omega, T) = \frac{c_0(r, T)}{\omega} + c_1(r, T)\omega + c_2(r, T)\omega^3 + \dots \quad (18)$$

We emphasize that Eq. (17) is a completely nonperturbative parametrization. The only information we take from HTL perturbation theory is the possible  $\tau$  dependence, which can give rise to the limit in Eq. (13).

Using this form of  $\eta_r(\omega)$ , the  $\tau$  dependence of the integration in Eq. (14) can be computed and we obtain the following expression for the Wilson line correlator:

$$\begin{aligned} \log W(r, \tau, T) &= -\Omega(r, T)\tau + \frac{c_0(r, T)}{\pi} \log[\sin(\pi\tau T)] \\ &+ \sum_{l=1}^{\infty} \frac{c_{l+1}(r, T)}{\pi} (2l-1)! T^{2l} (\zeta(2l, \tau T) \\ &+ \zeta(2l, 1 - \tau T)) + \text{const}(r, T). \end{aligned} \quad (19)$$

Using this HTL parametrization it is easy to check that the limit in Eq. (13) exists and the static energy is given by

$$E_s(r, T) = \lim_{t \rightarrow \infty} i \frac{\log W(r, t, T)}{\partial t} = \Omega + ic_0 T. \quad (20)$$

From this equation we can identify the imaginary part of the static energy  $\Gamma(r, T) = -c_0 T$ . Furthermore, at large Minkowski time higher-order terms,  $l \geq 1$ , do not contribute, i.e., the large Minkowski time behavior of  $W(r, t, T)$  is determined by  $\Omega$  and  $c_0$ , which in this case can be identified with the real and imaginary parts of the static energy.

It has been found in Ref. [24] for quenched QCD with an unimproved gauge action and large  $N_\tau$  that with the expression in Eq. (19), which is motivated from leading-order HTL perturbation theory, a reasonable number of data points around  $\tau \sim 1/(2T)$  could indeed be described by the above expression. However, with  $N_\tau = 12$  the number of data points available for fitting near  $\tau \sim 1/(2T)$  becomes small.

If we focus on the narrow region around  $\tau = 1/(2T)$ , and if the higher order terms in Eqs. (18) and (19) can be

neglected, we can fit the lattice results on the first moment with the form

$$\begin{aligned} m_1(r, n_\tau = \tau/a)a &= \log \left( \frac{W(r, n_\tau, N_\tau)}{W(r, n_\tau + 1, N_\tau)} \right) \\ &= \Omega(r, T)a - \frac{\Gamma(r, T)a N_\tau}{\pi} \log \\ &\times \left[ \frac{\sin(\pi n_\tau / N_\tau)}{\sin(\pi(n_\tau + 1)/N_\tau)} \right]. \end{aligned} \quad (21)$$

We performed fits of our  $N_\tau = 12$  lattice data for  $m_1$  for  $\tau/a = 5, 6, 7$  using Eq. (21) to determine  $\Omega(r, T)$  and  $\Gamma(r, T)$ . The details of these fits can be found in Appendix C.

A sample fit for both unsubtracted and subtracted data is shown in Fig. 11. The ansatz also describes some data points outside the fitting range. The smaller  $\tau$  and larger  $\tau$  behavior are not expected to be described by the above ansatz, as it only describes the dominant peak of the spectral function. In Fig. 12 we show  $\Omega(r, T)$  and  $\Gamma(r, T)$  from these fits as functions of  $r$  at different temperatures. The peak position  $\Omega(r, T)$  and width  $\Gamma(r, T)$  for subtracted and unsubtracted correlators are very close to each other. This is expected because we only consider  $\tau$  values around  $1/(2T)$ , where the

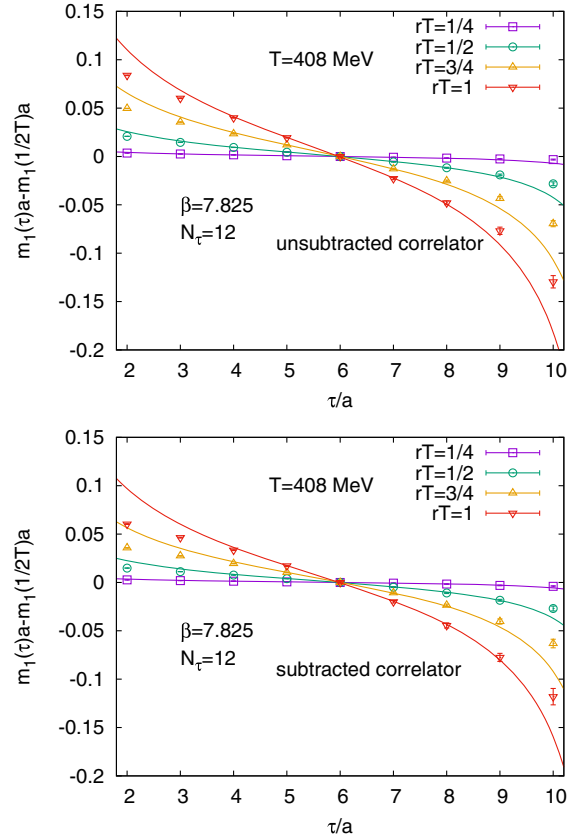


FIG. 11. Sample fit of the lattice result (top) unsubtracted correlator and (bottom) subtracted correlator to Eq. (21) (see text).

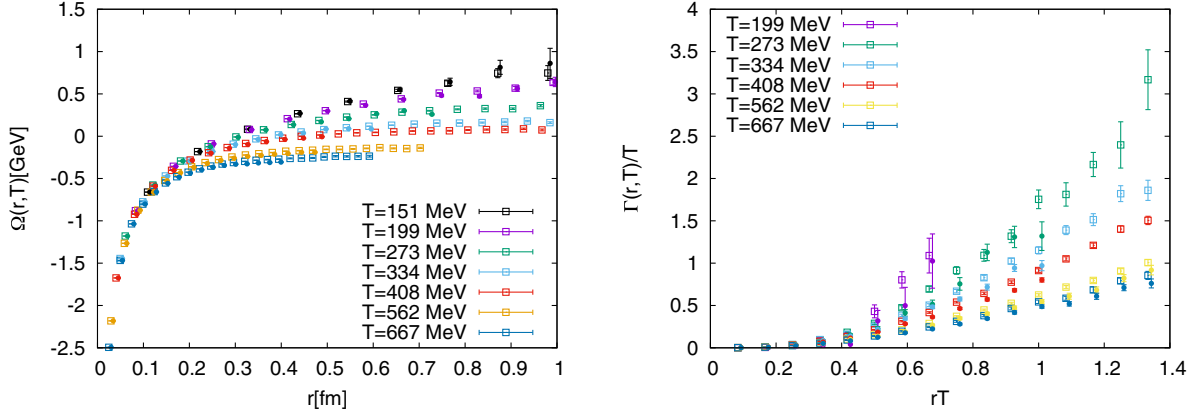


FIG. 12. The peak position (left) and the width (right) from the HTL-motivated method as functions of  $r$  at different temperatures. The open (closed) symbols correspond to real and imaginary parts from the unsubtracted (subtracted) correlator.

contribution of the high  $\omega$  part of the spectral function is small. The peak position,  $\Omega(r, T)$  shows significant temperature dependence and differs from the zero temperature potential. The width of the peak,  $\Gamma(r, T)$  increases with increasing  $r$ . Furthermore,  $\Gamma(r, T)$  does not scale with the temperature unlike in the case of Gaussian fits in the temperature range explored by us. We also find that in the temperature region studied by us  $\Gamma(r, T)$  is larger than the HTL result.

Another widely studied quantity at finite temperature is the singlet free energy  $F_S(r, T)$ ; see e.g., Ref. [7]. As mentioned above in leading-order HTL perturbation theory, the singlet free energy and the real part of the static energy are the same. From Fig. 13 we see that even nonperturbatively the difference between  $\Omega(r, T)$  and  $F_S(r, T)$  is very small, while the difference between the zero temperature static energy and  $F_S(r, T)$  is even smaller for  $rT < 0.4$  [7]. This is very similar to the findings of the calculations in quenched QCD, where smeared Wilson loops have been used [24].

It is straightforward to continue the parametrization of the Wilson line correlator given by Eq. (19) to Minkowski

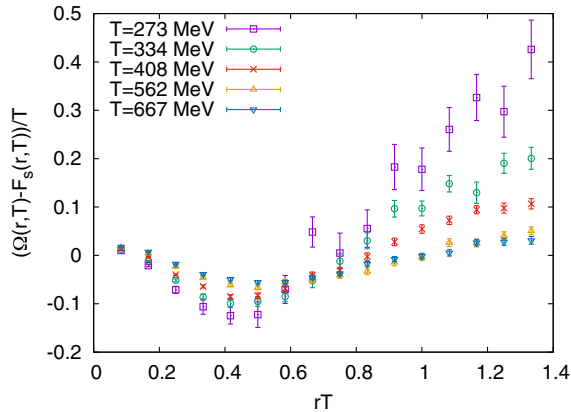


FIG. 13. The difference between the peak position  $\Omega(r, T)$  and singlet free energy  $F_S(r, T)$  at different temperatures.

time and then calculate the dominant peak of the spectral function  $\rho_r^{\text{med}}(\omega, T)$ ,

$$\rho_r^{\text{med}}(\omega, T) = \int_{-\infty}^{\infty} W(r, t, T) \exp(i\omega t) dt, \quad (22)$$

which is plotted in Fig. 14. The dominant peak looks qualitatively similar to the leading-order HTL spectral function; see Fig. 6.

We would like to again mention that the spectral feature  $\rho_r^{\text{med}}(\omega, T)$  plotted in the figure is not the full spectral function  $\rho_r(\omega, T)$ , but rather the dominant peak of  $\rho_r^{\text{med}}(\omega, T)$  due to the thermal static energy.  $\rho_r^{\text{med}}(\omega, T)$  is quite different from the full spectral function  $\rho_r(\omega, T)$  for  $\omega$  far away from its peak at  $\Omega(r, T)$ . A similar situation also arises while calculating the  $Q\bar{Q}$  potential in the hadronic phase. In this case it is well known that the dominant peak of the spectral function is the Dirac delta function, and this describes only the plateau region of  $m_1$ .

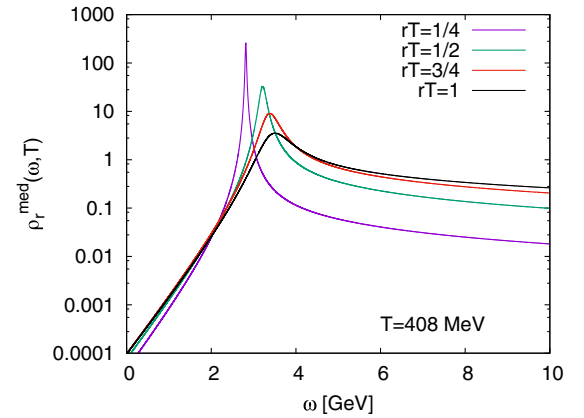


FIG. 14. Dominant peak of the spectral function for  $T = 408$  MeV at various distances from the HTL-motivated method.

The integration in Eq. (22) can be performed exactly [56] and near the peak, where  $\rho_r^{\text{med}}(\omega, T)$  describes the spectral function reliably, it can be approximated by

$$\rho_r^{\text{med}}(\omega, T) \approx \sqrt{\frac{2}{\pi}} \frac{\Gamma(r, T)}{(\Omega(r, T) - \omega)^2 + \Gamma(r, T)^2} \times |\Omega(r, T) - \omega|, \quad \Gamma(r, T) \ll T. \quad (23)$$

This is expected as we already assumed the limit in Eq. (13) exists.

### C. Determining the ground state peak via the Padé rational approximation

So far we have used two methods to extract the properties of the ground state spectral peak, which both required some form of modeling input. In the spectral fit approach it amounts to the choice of fitting with a spectral function for which the second moment is much larger than the higher moments. A Gaussian shape for the dominant peak and a number of supporting delta peaks is one possible such choice. In the Bala-Datta method of Ref. [24] the applicability of a nonstandard spectral representation [see Eq. (14)] is assumed. Here we attempt to extract the potential with a model independent approach, based on the Padé rational approximation. One reason to deploy the Padé rational approximation is that for the Symanzik gauge action, the spectral function of the Wilson line correlator (or Wilson loop) is not positive for large  $\omega$  when the separation,  $r$  is small as discussed in Ref. [43]. Thus Bayesian approaches designed to operate on positive spectral functions, deployed in the past, may not be reliable on this data set. We see that at high temperatures and small separation distances the Bayesian approaches indeed fail when applied to the raw data.

In the Padé approach we first transform the Euclidean correlator data into Matsubara frequency space, after which we carry out a projection of the data onto a set of rational basis functions, which are then analytically continued. From the ensuing correlation functions in real-space frequencies, the spectral functions are obtained by taking the negative of the imaginary part, drawing on the analytic properties of the Lehmann representation

$$W(r, \tilde{\omega}_n, T) = \int d\omega \frac{1}{\omega - i\tilde{\omega}_n} \rho_r(\omega, T). \quad (24)$$

The Wilson line correlator is particularly well suited in this context. Since it does not contain the cusp divergences that plague the Wilson loop, approximations that exploit analyticity, such as the Padé approximation, are expected to work well.

Since the analytic continuation of a Padé approximation of a lattice correlator is known to require extremely precise data to yield robust results—often beyond what a lattice

simulation can provide in practice—it has not been commonly deployed for spectral function reconstruction so far (for recent work see e.g., Ref. [57]). In addition it is known that the Padé approximation does not respect the spectral representation of the input data (see e.g., Ref. [58]), i.e., the reconstructed spectral function inserted into Eq. (24) does not necessarily reproduce the input data.

All direct projection methods, such as e.g., those by Cuniberti [59], suffer from the fact that, in contrast to the Bayesian approach, the influence of the data uncertainty on the projection is not regularized. On the other hand the Padé method has an advantage over the Bayesian approach in that it can exploit much more efficiently the smallness of statistical error bars. In the Bayesian approach, reducing the statistical uncertainty, while leaving the number of data points fixed may result in increased ringing artifacts in practice, an issue that the Padé approximation does not suffer from in the same manner. And it is the exceptionally high statistics of the ensembles present in this study that promise that a meaningful Padé approximation can be carried out, as we will show in the following.

In this study we implement the Padé approximation in the form of a continued fraction according to the Schlessinger prescription [60]. This particular approach amounts to a Padé approximation in which the polynomial in the denominator carries at least the same order as that in the numerator or one higher order, leading to an expression that is able to robustly reproduce functions that decay at large frequencies, which is just the case for the Wilson line correlator [37]. Note that it actually amounts to an interpolation of the data, which in contrast to a fitted rational approximation does not require us to carry out a costly minimization. We deploy the approximation on the Wilson line correlators in imaginary frequency space

$$W(r, \tilde{\omega}_n, T) = \sum_{j=0}^{N_\tau-1} e^{ia\tilde{\omega}_n j} W(r, ja, T), \quad \tilde{\omega}_n = 2\pi n/aN_\tau. \quad (25)$$

A representative example is shown in Fig. 15, where we plot as discrete data points in the top panel the real part and in the bottom panel the imaginary part of the correlator at  $T = 408$  MeV ( $\beta = 7.825$   $N_\tau = 12$ ) at three spatial distances  $r = 0.0387$  fm,  $r = 0.176$  fm and  $r = 0.296$  fm (dark blue to light blue).

Note that the discrete Fourier transform (DFT) applied to Eq. (25) does not reproduce the continuum Lehmann kernel but introduces corrections related to both the finite lattice spacing and available grid size. Since our subsequent strategy to extract the spectral function will rely on the continuum form of the Lehmann representation, we need to compensate for these artifacts, which we do in the spirit of the tree-level corrections of the lattice artifacts in the static  $Q\bar{Q}$  energy [61], i.e., instead of using the naive Fourier

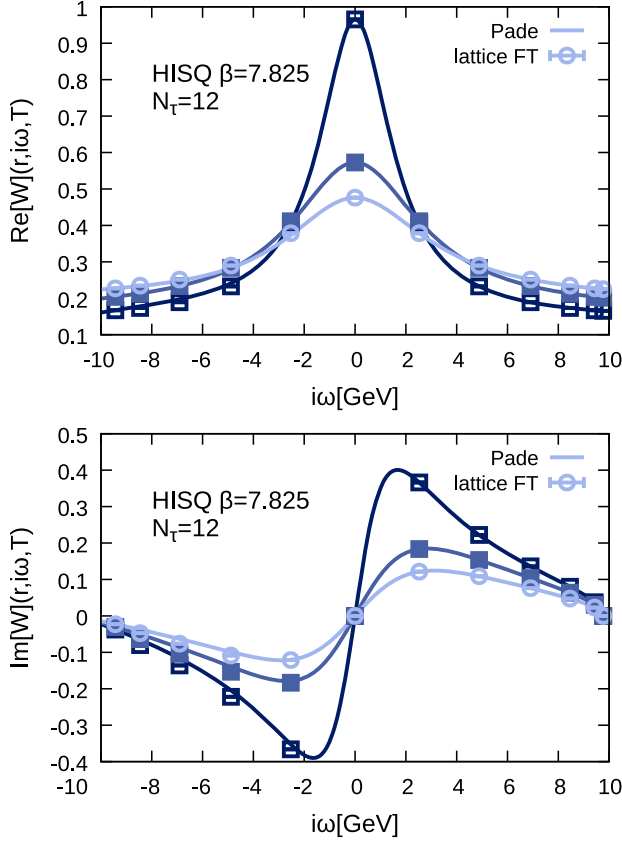


FIG. 15. Discrete Fourier transform of the  $T > 0$  Wilson line correlators at  $T = 407$  MeV ( $\beta = 7.825$ ,  $N_\tau = 12$ ) at three spatial separation distances  $r = 0.03872$  fm,  $r = 0.1758$  fm and  $r = 0.2964$  fm. The top panel shows its real part, while the lower panel its imaginary part as colored symbols. The solid lines denote the Padé approximation based on eight data points, which is subsequently used in the analytic continuation.

frequencies  $\tilde{\omega}_n$ , we instead assign the Matsubara correlator data points to the eigenvalues of the discrete frequency operator

$$\tilde{\omega}_n \rightarrow \omega_n = 2 \sin\left(\frac{\pi n}{N_\tau}\right)/a. \quad (26)$$

The  $\omega_n$  absorb the distortion of the frequency Brillouin zone in the UV and we may interpret the correlator as being expressed otherwise in its continuum form (we have checked that taking into account the DFT artifacts improves the stability of the Padé extraction using mock data). The deployment of the corrected frequencies also means that our correlators are plotted on nonequidistant frequency values in Fig. 15.

With the Wilson line correlators not being symmetric in Euclidean time, their discrete Fourier transform is in general complex valued. The complex data along the corrected imaginary frequencies  $\omega_n$  is interpolated by a continued fraction  $C_{N_\tau}$  of the form

$$\begin{aligned} C_{N_\tau}(r, i\omega, T) &= \frac{W(r, \omega_0, T) a_0(r, T) [\omega - \omega_0] a_1(r, T) [\omega - \omega_1]}{1 + \frac{a_{N_\tau-2}(r, T) [\omega - \omega_{N_\tau-2}]}{1 + a_{N_\tau-1}(r, T) [\omega - \omega_{N_\tau-1}]} \dots} \quad (27) \end{aligned}$$

For better readability the above continued fraction is expressed in the following way: each subsequent level of the continued fraction, instead of being written in the denominator of the preceding term, is listed as a separate fraction to the left. The expression  $1+$  in the denominator therefore indicates that the following fraction should be considered the next level of the continued fraction; concretely  $\frac{A}{1+\frac{B}{1+C}} \equiv (A/(1+(B/(1+C))))$ .

The complex coefficients are determined recursively by demanding that the rational approximation exactly reproduces the input data at each available frequency, leading to the following prescription:

$$\begin{aligned} a_l(r, T) (\omega_{l+1} - \omega_l) &= - \left\{ 1 + \frac{a_{l-1}(r, T) [\omega_{l+1} - \omega_{l-1}] a_{l-2}(r, T) [\omega_{l+1} - \omega_{l-2}] \dots}{1 + \frac{a_0(r, T) [\omega_{l+1} - \omega_0]}{1 - [W(r, \omega_0, T)/W(r, \omega_{l+1}, T)]}} \right\}. \quad (28) \end{aligned}$$

Applying this formula directly to complex valued imaginary frequency data amounts to a generalization of the resonances via the Padé method used e.g., in Ref. [62] to nonsymmetric correlators in Euclidean time. The evaluation of a continued fraction is prone to the accumulation of rounding errors, which is why we compute the  $a_i$ 's with at least 30-digit accuracy. This need for accuracy is independent of the amount of noise present in the underlying data and is a well known drawback of direct projection methods [59]. The outcome of the interpolation, based on a subset of eight input data points (the seven positive Matsubara frequency data points and the one at the smallest negative available frequency), is shown as solid colored lines in Fig. 15. Substituting in the continued fraction the Euclidean frequencies by their Minkowski counterparts  $C_{N_\tau}(r, i\omega, T) \rightarrow C_{N_\tau}(r, \omega, T)$  we explicitly implement the analytic continuation.

There are two equivalent ways to proceed. We may either compute the spectral function from  $C_{N_\tau}(r, \omega, T)$  via the real-time relation

$$\rho_r(\omega, T) \approx -\frac{1}{\pi} \text{Im}[C_{N_\tau}(r, \omega, T)] \quad (29)$$

and carry out a similar analysis as that in previous studies based on Bayesian spectral reconstructions. In that approach we locate the lowest lying peak structure in

$\rho_r(\omega, T)$  and fit it with a skewed Lorentzian, embedded in a polynomial background of the form derived in Ref. [63]

$$\begin{aligned} \rho_r(\omega, T) &\propto \frac{|\Gamma(r, T)| \cos[\text{Re}\sigma_\infty(r, T)] - (\Omega(r) - \omega) \sin[\text{Re}\sigma_\infty(r, T)]}{\Gamma(r, T)^2 + (\Omega(r) - \omega)^2} \\ &+ c_0(r, T) + c_1(r, T)(\Omega(r, T) - \omega) \\ &+ c_2(r, T)(\Omega(r, T) - \omega)^2 \dots \end{aligned} \quad (30)$$

On the other hand we may ask whether the information encoded in the dominant spectral peak may be read off from the real-time correlator directly in a more simple fashion. Indeed the peaks of the spectral function are but a projection of the pole structure of the underlying correlation function. Since we are in possession of the rational function approximation of the correlator, we can compute the pole structure explicitly from the roots of the polynomial in the denominator. The number of poles present, obviously depends on the degree of the Padé interpolation, but we find that varying the number of input points does not change the fact that one of the poles lies significantly closer to the real frequency axis than all other poles. This pole in turn leads to the dominant peak structure seen in the spectral function. We have checked that both approaches give numerically consistent results for the position and width of the dominant spectral peak and therefore in the remainder of the study will analyze the spectrum directly via the poles.

In order to ascertain, whether the Padé approximation is a viable method for the exploration of spectral structures in practice we must assess its reliability in a realistic test scenario. To this end we carry out mock data tests based on HTL correlation functions. We deploy as a starting point the ideal correlators computed for  $T = 667$  MeV, discretized on  $N_\tau = 12$  points. This ideal data is distorted by Gaussian noise. Here 1000 samples of the correlator are generated, such that their mean exhibits constant relative uncertainties of either  $\Delta D/D = 10^{-2}$  or  $\Delta D/D = 10^{-3}$ . Since the data in our lattice study is precise down to the subpercent level, the choice of one-percent relative error corresponds to a worst case scenario for the Padé analysis, while the one-per-mille error represents the best-possible scenario.

We carry out the Padé interpolation and pole analysis based on a selection of eight noisy input data points, starting with the correlator at positive Matsubara frequencies. We have checked that adding or removing two data points does not significantly change the results, as well as that a reordering of the data points in the construction of the continued fraction does not have any relevant effects. Note that when adding more and more data points in the construction of the Padé approximation, it will eventually become unreliable. The reason is that the redundancy of the Matsubara input data (symmetry of  $\text{Re}[W]$ ,

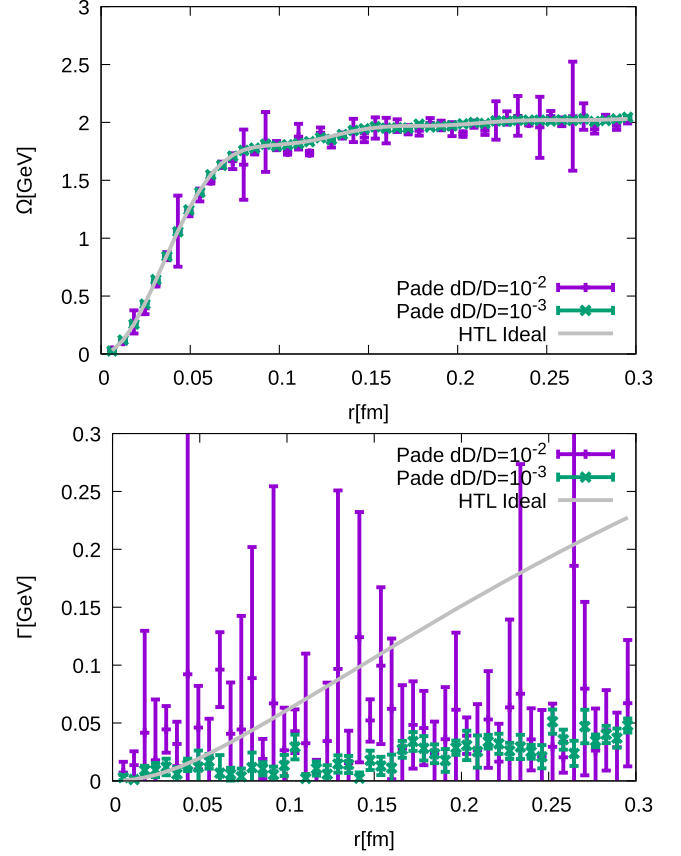


FIG. 16. Extraction of spectral position  $\Omega$  and width  $\Gamma$  of the dominant peak, based on hard thermal loop mock data for  $dD/D = 10^{-2}$  and  $dD/D = 10^{-3}$  for  $T = 667$  MeV. The error bars are obtained from jackknife resampling.

antisymmetry of  $\text{Im}[W]$ ) requires subtle cancellations to take place in the continued fraction. We found that if we use  $N_\tau/2 + 2$  data points for the approximation, the position of poles does not change beyond statistical errors with addition or removal of one more data point. Thus, the optimal choice for stability was found when using  $N_\tau/2 + 2$  data points.

The real and imaginary parts of the dominant pole are plotted in the top and bottom panels of Fig. 16 respectively as colored data points. The analytically known values for the peak position  $\Omega$  and its width  $\Gamma$  are shown as gray solid lines. The error bars here arise from a combination of jackknife uncertainty, the differences in changing the number of data points by one or two, as well as the reordering in the construction of the continued fraction.

The HTL Padé pole analysis is very encouraging in that even under the adverse circumstances of the relatively large statistical uncertainty of  $\Delta D/D = 10^{-2}$  it allows us to recover the position of the dominant peak well within uncertainties. For  $\Delta D/D = 10^{-3}$  the results are spot on.

In Fig. 17 we have also computed several spectral functions for  $\Delta D/D = 10^{-3}$ . We can see that the peak position is very well estimated. As expected the

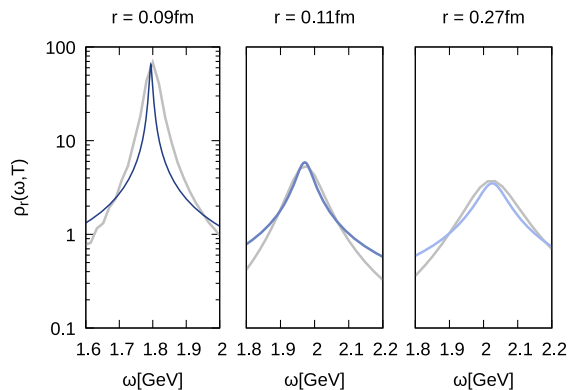


FIG. 17. Representative selection of spectral functions extracted from hard thermal loop ideal data for  $dD/D = 10^{-3}$  at  $r = 0.09, 0.11$  and  $0.27$  fm respectively using Padé (colored lines) vs the analytic HTL result (gray lines).

determination of the spectral width  $\Gamma$  on the other hand is much more difficult and for the small number of data points present here ( $N_\tau = 12$ ), the results are not yet robust at  $\Delta D/D = 10^{-2}$  and tend to significantly underestimate the true value even for  $\Delta D/D = 10^{-3}$ . Thus for the application to actual lattice data we will focus on extracting  $\Omega$  in the following.

Having checked the limitations of the Padé method in a nontrivial realistic test case, we proceed to apply it to our HISQ lattice data. We have carried out the pole analysis for Padé interpolations based on different numbers of input data points. On  $N_\tau = 12$  lattices the results are unaffected by changing between seven to eleven input points and we arbitrarily decide to show the results based on eight. The uncertainty budget represented by the error bars includes the jackknife errors, as well as variation due to changes in the ordering when composing the continued fraction.

For the  $N_\tau = 12$  lattices we investigated, the Padé interpolation yields one dominant pole close to the real

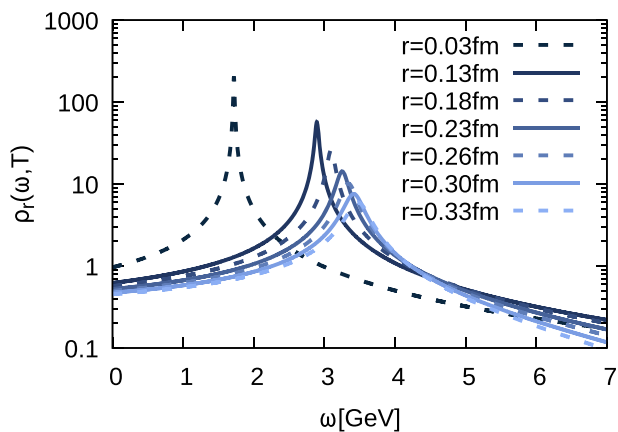


FIG. 18. Representative spectral functions obtained from the Padé interpolation at  $T = 407$  MeV ( $\beta = 7.825$   $N_\tau = 12$ ) for different separation distances. A single well defined peak structure of skewed Lorentzian form emerges from the analysis.

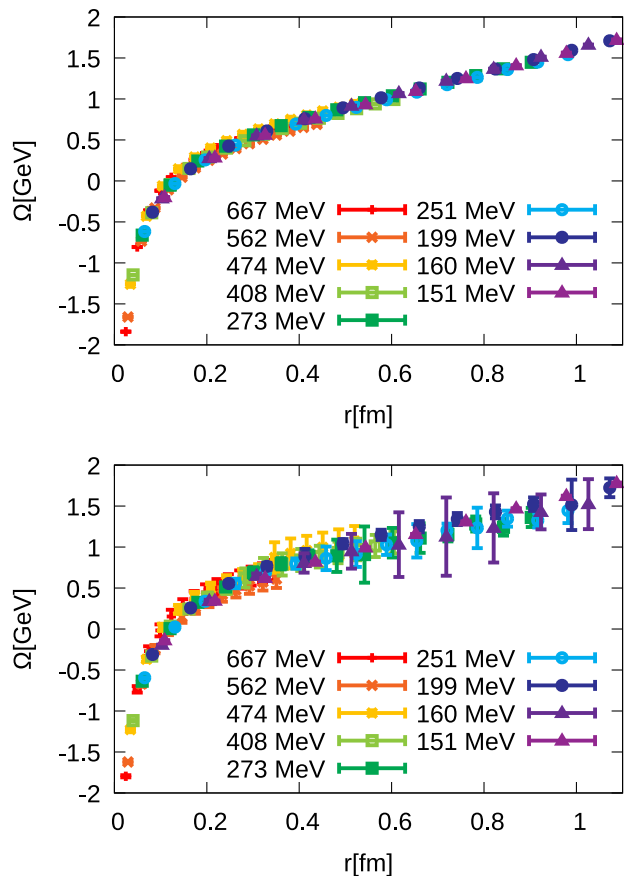


FIG. 19.  $\Omega$  as a function of separation distance for different temperatures obtained from a Padé pole analysis on  $N_\tau = 12$ . The figure on the top is obtained by using the unsubtracted correlator and the figure on the bottom is obtained using the subtracted correlator.

axis manifesting itself as a well-defined skewed Lorentzian peak in the spectral function, as shown in Fig. 18. Following the same procedure as in the HTL mock data test, we can read of the real-part of the pole as  $\Omega$  plotted in Fig. 19 and the imaginary part as  $\Gamma$  shown in Fig. 20. As the HTL mock data analysis suggests that a reliable reconstruction of the potential's imaginary part is not possible even with smaller errors than what we presently have from the lattice, we present the values of  $\Gamma$  reconstructed from the lattice data simply for completeness. We have carried out the analysis on both the subtracted and unsubtracted correlators (see Sec. III B) and found that the subtracted correlators are computed to a statistical precision which unfortunately is not high enough for the Padé approximation to extract the value of  $\Gamma$  with even statistical reliability.

The values the Padé analysis yields for  $\Omega$  on the HISQ Wilson line correlators are similar to the results obtained from the model spectral function fits deployed in Sec. IV A. We find that the values do not show any significant changes over a large temperature range.

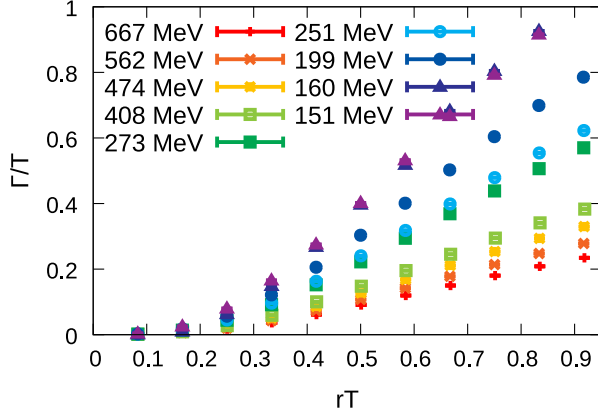


FIG. 20. Width  $\Gamma$  as a function of separation distance for different temperatures obtained from Padé pole analysis for  $N_\tau = 12$ . The analysis is done using unsubtracted correlators.

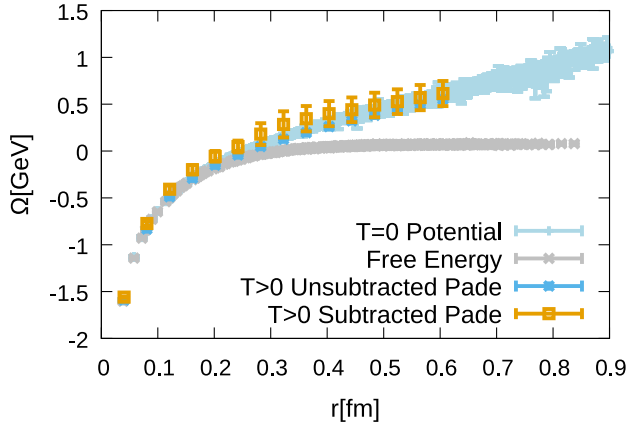


FIG. 21. Comparison of extracted  $\Omega$  using subtracted and unsubtracted correlators using Padé pole analysis with the  $T = 0$  effective mass and color singlet free energy at  $T = 408$  MeV ( $\beta = 7.825$ ,  $N_\tau = 12$ ).

In Fig. 21 we pick out the results at  $T = 407$  MeV for a closer inspection. We plot  $\Omega$ , based on the subtracted and unsubtracted Euclidean correlator Padé analysis at  $T > 0$  (orange and dark blue data points), along with the  $T = 0$  static energy (light blue data points) and the color singlet free energy. The results obtained are in stark contrast to those of the method by Bala and Datta, in which at temperatures inside the quark-gluon plasma (QGP) phase one does observe a deviation from the linear rise present in the hadronic phase. Our Padé results appear also in stark contrast to previous analyses of the spectral functions of Wilson lines from both quenched [19,21] and dynamical QCD [22,23] based on Bayesian methods. There a discernable change of  $\Omega$  with temperature was found, more similar to the results of the HTL-motivated method in this study. A previous Padé analysis of a subset of the HISQ data was discussed in Ref. [64]. That analysis showed relatively large uncertainties, arising from the fact that less statistics was available and that the improved frequencies

were not deployed. Within its sizable uncertainties, these results were consistent with the Bayesian studies but within  $2\sigma$  would also encompass the result obtained here.

#### D. Determining the ground state peak via Bayesian reconstruction

The last type of methods to be deployed in the study of the Wilson line spectral function are Bayesian spectral reconstructions. While the most well known variant, the maximum entropy method [65] faces challenges, as it does not easily reproduce Lorentzian structures encoded in peaks, the more recently developed BR method [19] has been deployed successfully in the extraction of such structures, both from mock data as well as from lattice QCD data.

All Bayesian methods exploit Bayes' theorem

$$P[\rho|D, I] \propto P[D|\rho, I]P[\rho|I] = \exp[-L + \alpha S_{\text{BR}}], \quad (31)$$

to systematically regularize the inversion problem. They amend the simulation data  $D$  by additional so called prior information  $I$ . The posterior probability  $P[\rho|D, I]$  for a test function  $\rho$  denotes the probability for  $\rho$  to be the correct spectrum, given simulation data and prior information, which in turn is written as the product of the likelihood  $P[D|\rho, I]$  and prior probability  $P[\rho|I]$ . The former states how compatible  $\rho$  is with the simulation data, and is nothing but the usual quadratic distance functional used in  $\chi^2$  fitting

$$L = \frac{1}{2} \sum_{i,j=1}^{N_d} (D_i - D_i^\rho) C_{ij}^{-1} (D_j - D_j^\rho). \quad (32)$$

Here  $C_{ij}$  denotes the standard unbiased covariance matrix. It is amended by the prior probability  $P[\rho|I] = \exp[\alpha S_{\text{BR}}]$ , which acts as a regulator to the many flat directions of the likelihood functional

$$S_{\text{BR}} = \int d\omega \left( 1 - \frac{\rho(\omega)}{m(\omega)} + \log \left[ \frac{\rho(\omega)}{m(\omega)} \right] \right). \quad (33)$$

The function  $m(\omega)$  denotes the default model and by definition corresponds to the correct spectrum in the absence of data. In this work, we choose to use a default model, which implements a  $1/\omega$  falloff at large frequencies as  $m(\omega) \propto 1/(a\omega - a\omega_{\text{min}} + 1)$ . When estimating the error budget for the spectral features we include the variation between results based on different default models, including the constant one, as well as  $m \propto \omega$ ,  $\omega^2$  and  $m \propto 1/(a\omega - a\omega_{\text{min}} + 1)^2$ .

In the original formulation of the BR method, the hyperparameter  $\alpha$ , which weighs the influence of prior information and data is marginalized from the posterior by assuming no knowledge of its values  $P[\alpha] = 1$  so that

$$P[\rho|D, I, m] \propto P[D|\rho, I] \int_0^\infty d\alpha P[\rho|m, \alpha] P[\alpha]. \quad (34)$$

In this study we deploy a different handling of  $\alpha$ , namely we tune the hyper parameter such that the likelihood takes on the value  $L = N_\tau/2$ . This procedure is similar to applying the Morozov criterion in classic regularization. The motivation for this choice is to avoid very large or very small values of  $\alpha$  to contribute to the end results, as would be the case when integrating over  $P[\alpha] = 1$ . In turn the occurrence of ringing artefacts is expected to be diminished. In the present study no significant differences between different choices of  $\alpha$  handling were found.

After specifying the likelihood and prior, we numerically search for the most probable spectrum in the Bayesian sense by locating the unique extremum of the posterior  $P[\rho|D, I, m]$  via a quasi-Newton optimization algorithm, the Limited Memory Broyden–Fletcher–Goldfarb–Shanno method. In practice we resolve the spectrum along  $N_\omega = 1000$  points in a frequency interval of  $\omega a = [0:15]$ . We take into account all Euclidean data points except at  $\tau = 0$  and  $\tau = 1/T$ . This in particular excludes the point from which the color singlet free energies are defined.

In previous studies it has been observed that the BR method is well suited to extract strongly peaked spectral features with high accuracy. On the other hand, if only a small number of data points are available  $O(10)$ , the regulator  $S_{\text{BR}}$  is unable to avoid ringing artifacts in the reconstruction if the encoded spectrum contains broad structures. Improving the regulator functional to retain its resolving capability, while preventing ringing is a work in progress (see e.g., Ref. [66]).

We can benchmark the reliability of the spectral reconstruction at high temperatures by using the nontrivial mock data computed in HTL similarly as for the Padé reconstruction. In this case we add Gaussian noise with constant relative error  $\Delta D/D = \kappa = \text{const}$  directly to the Euclidean data and supply it to the reconstruction algorithm. As shown in Fig. 22 we find that for the worst case test with  $\kappa = 10^{-2}$ , we are able to reproduce the position of the lowest lying peak with higher precision than what the Padé method allows us to do. For the width  $\Gamma$ , the BR results at  $\kappa = 10^{-2}$  are equally disappointing as with the Padé method. However if we go to the best case scenario of  $\kappa = 10^{-3}$ , the BR method shows its strength in being able to much more closely recover the correct imaginary part compared to the Padé method.

It is important to note that in none of the HTL mock data tests have we encountered any signs of ringing artifacts. This combined with the fact that the imaginary part of the HTL potential is reproduced well, implies that the BR method is well suited for reconstructing positive definite spectral functions. A representative selection of reconstructed spectral functions obtained with the BR method from HTL mock data is shown in Fig. 23.

At low temperatures, e.g., at  $T = 151$  MeV, the Euclidean correlators do not yet show signs of positivity violation (i.e., we obtain effective masses that are monotonic in Euclidean time) and the BR method succeeds in

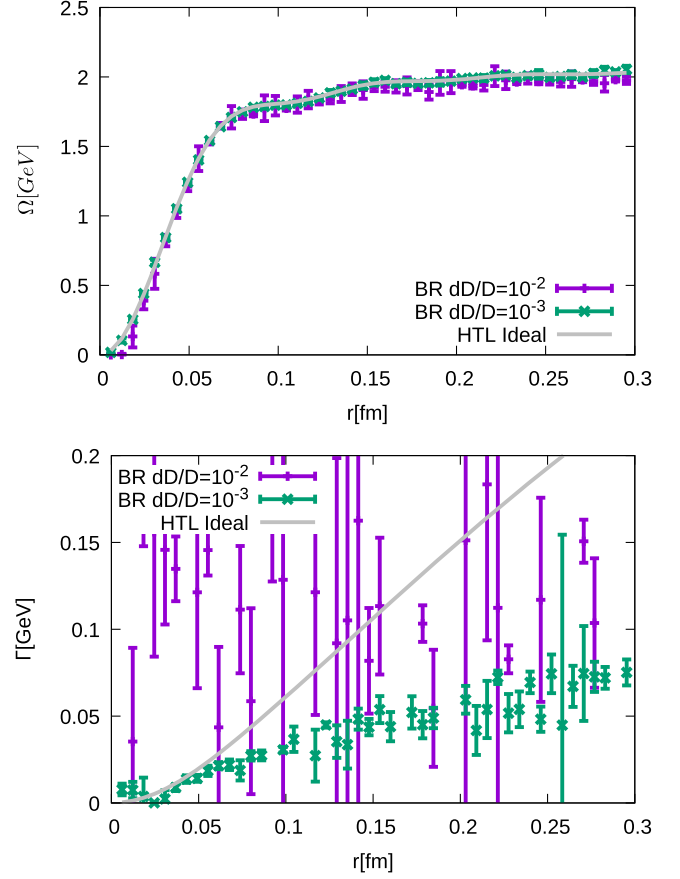


FIG. 22. Extraction of  $\Omega$  and width  $\Gamma$  for hard thermal loop ideal data for  $dD/D = 10^{-2}$  and  $dD/D = 10^{-3}$  for  $T = 667$  MeV using the BR method. The error bars are obtained from jackknife resampling.

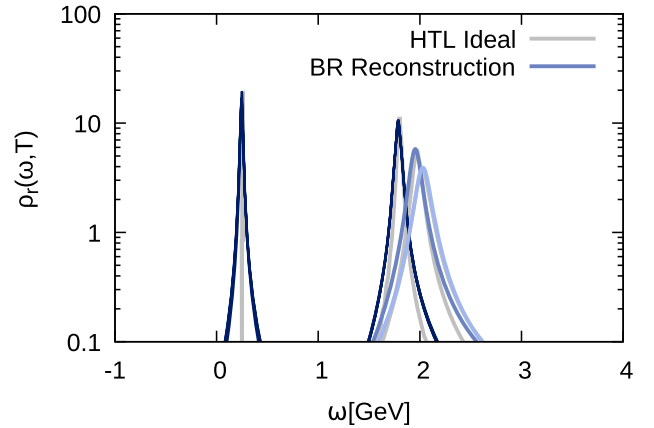


FIG. 23. A selection of spectral functions extracted from hard thermal loop data for  $dD/D = 10^{-3}$   $r = 0.01, 0.09, 0.11$  and  $0.27$  fm respectively (dark blue to light blue) using Bayesian reconstruction vs the analytic result (solid gray).

reconstructing their spectral function. By construction, the result reproduces the input Euclidean data points within their statistical errors. A selection of these spectra for  $r = 0.32, 0.64, 0.96$  and  $1.28$  fm is shown in Fig. 24 (solid dark blue to

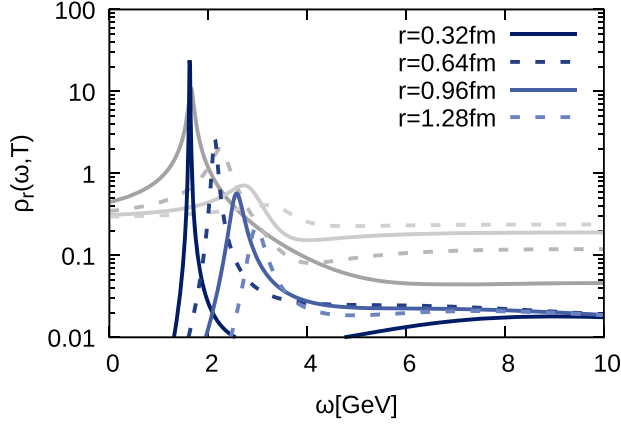


FIG. 24. Comparison of reconstructed spectra using the Padé (grey) and BR (blues) methods at  $T = 151$  MeV ( $\beta = 6.740$ ,  $N_\tau = 12$ ) at different separation distances  $r = 0.32, 0.64, 0.96$  and  $1.28$  fm.

lighter blue) compared to the outcome of the Padé reconstruction (gray solid).

We find important differences between the two approaches. The BR method reconstructions, as expected from the effective mass analysis, show a single well defined lowest lying peak. Towards the origin that peak rapidly decays in an exponential fashion, which is qualitatively similar to the behavior observed in HTL spectral functions. In contrast the Padé reconstruction assigns significant weight to the low frequency region. This difference is among the reasons, why the spectral function of the Padé reconstruction does not fulfill the spectral decomposition of the original Euclidean data, a known drawback of the Padé reconstruction method.

At larger frequencies than its maximum, the BR spectral function shows a tail, which eventually behaves as the underlying default model, i.e.  $\propto 1/\omega$  for our main choice. We have checked that changing the default model to different powers  $\alpha$  as  $m \propto \omega^\alpha$  does not change the peak structure significantly. The central peak obtained by the BR method agrees in position with the Padé result at small distances. At larger distances the Padé method finds a bump that is broadened considerably and assumes its maximal value at a higher frequency than the BR spectra peak.

Let us compare  $\Omega$  obtained from the Padé pole analysis (magenta) and the skewed Breit-Wigner fit of the BR spectral reconstruction (light blue) in Fig. 25. In addition we provide the values of the peak position  $\Omega$  at  $T = 0$  in green. Since  $T = 151$  MeV still lies close to the crossover transition, the effect of the medium on the static potential is expected to be weak. We find this intuition reflected in the agreement between the zero temperature static energy and the BR result for  $\Omega$ . Interestingly all three results agree up to around  $r = 0.3$  fm. However as we consider larger distances we find that the Padé reconstruction shows a systematic tendency to lie above the zero temperature static energy. The effect becomes significant around  $r = 0.5$  fm and remains visible

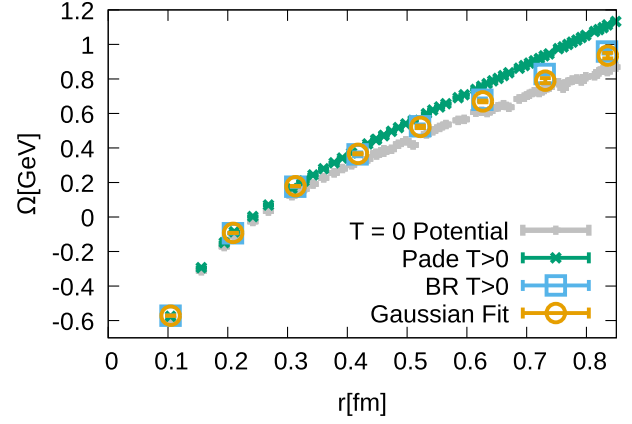


FIG. 25. Comparison of  $\Omega$  using the Padé method, BR method and Gaussian fit at  $\beta = 6.740$  with  $N_\tau = 12$  ( $T = 151$  MeV). The  $T = 0$  potentials for the same  $\beta$  are given as grey data points.

up to  $r = 0.85$  fm, beyond which the signal of the  $T = 0$  static energy is lost. The BR result lies much closer to the  $T = 0$  effective masses over the whole range of distances.

The success of the BR reconstruction at  $T = 151$  MeV tells us that the data is compatible with a dominant skewed Breit-Wigner peak structure in the spectral function. At higher temperatures the BR method cannot be reliably applied to the extraction of spectral functions from the raw correlators, due to the presence of nonpositivity in the underlying spectral functions. At  $T = 407$  MeV, for example, the effective masses at small distances show explicitly nonmonotonic behavior [7]. However, the spectral density may not be positive definite even if the effective masses decrease monotonically. We see that also at intermediate distances, the BR method fails to converge successfully.

While in principle we could proceed by investigating the UV-subtracted finite temperature correlators, we have found that the statistical uncertainties introduced by the  $T = 0$  subtraction dominate over those inherent in the  $T > 0$  data, thus preventing us from a precision analysis of the spectral function at higher temperatures.

## V. CONCLUSIONS

In the first part of the study we have investigated the Wilson line correlation functions obtained from the numerical simulations directly in imaginary time. We computed the first three cumulants, as defined in Eq. (7), of the imaginary-time correlation functions. The  $n$ th cumulant of the imaginary-time correlation function at  $\tau = 0$  is equivalent to the  $n$ th moment of the corresponding spectral functions [see Eq. (3)], assuming that the moment of the underlying spectral functions is finite. We found that they differ beyond statistical errors from the predictions of resummed HTL perturbation theory at all temperatures investigated, including the highest temperature,  $T = 1938$  MeV. Furthermore, even at the qualitative level there is a difference between the

lattice results and HTL result. The first cumulant calculated in leading order HTL perturbation theory is antisymmetric around  $\tau = 1/(2T)$ , but the lattice results do not show such a feature except near  $\tau \sim 1/(2T)$ . In addition we checked that our data sets allow for a meaningful determination of up to the third cumulant of the correlation function in Euclidean time. For higher moments the signal to noise ratio does not suffice. In turn we understand that our input data will be able to constrain spectral information only within the limitations placed by these three moments.

The second part of the study was concerned with extracting the position  $\Omega$  and width  $\Gamma$  of the dominant spectral peak structure encoded in the Wilson line correlators. We deployed four different approaches: spectral function model fits where the dominant peak is described by a Gaussian, the HTL-inspired fit of Bala and Datta, the Padé approximation and, where positivity allowed, the BR method.

In essence each of the four methods introduces certain prior information in order to regularize the ill-posed inversion problem to gain access to the spectral function. It turns out that the Euclidean data scrutinized in the first part of our study is amenable to different possible hypotheses, which in turn lead to different outcomes for  $\Omega$  and  $\Gamma$ .

The spectral function fits assume that the high energy part of the spectral function has negligible temperature dependence, and that the observed temperature dependence of the Wilson line correlators is determined by the dominant peak structure. Since the correlator is found to have a second cumulant much larger than its higher cumulants, a Gaussian for the dominant peak, and a single delta function for the low energy tail are the simplest, permissible choices for parametrizing the data. The Gaussian spectral function model shows a value of  $\Omega$ , which is virtually independent of temperature and a width, which scales trivially with the temperature.

In order to extract the values of  $\Omega$  via the HTL-inspired fit, one assumes that the correlation functions are amenable to a certain nonstandard spectral decomposition, similar to the one encountered in leading-order HTL perturbation theory. This spectral decomposition leads to a first cumulant that is antisymmetric around  $\tau = 1/(2T)$ . Because of the small  $N_\tau$ , the fits can be performed only in a small region around  $\tau = 1/(2T)$ . This fit yields an  $\Omega$ , which shows clear temperature dependence and signs of asymptotic flattening in the QGP phase. The width that the method computes shows a nontrivial scaling with the temperature, which is weaker than linear in the temperature.

The third method we deployed is the Padé rational approximation. The only assumption it makes is that the correlation function represents an analytic function. However it suffers from the drawback that its outcome is known to violate the spectral decomposition of the input data. I.e., the Padé spectrum, when reinserted into the Lehmann representation, does not reproduce the original correlator. We have however tested the Padé method under

nontrivial settings in HTL perturbation theory and found that for the temperature and spatial separation distances probed, the position of the lowest lying peak structure was well reproduced. Applied to genuine lattice data we obtained results that were robust under changes in the number of input points and a reordering when constructing the Padé approximation of the Matsubara domain input data. The outcome of the extraction of  $\Omega$  based on the Padé method yields values, which similarly to the Gaussian model fit, show virtually no temperature dependence. While the mock data tests tell us to take the outcome of the width with a significant grain of salt, we find small statistical error bars and a behavior that qualitatively agrees with that of the Bala-Datta method, i.e.,  $\Gamma$  scales weaker than linear with the temperature.

Last but not least we also deployed the BR method, where positivity of the spectral function allowed. The BR method has been extensively tested on HTL mock data and has been shown to outperform other Bayesian methods, such as the maximum entropy method in the accurate reconstruction of the lowest lying peak from Wilson line correlators, a finding reproduced in this study. As the BR method is designed to reproduce the Euclidean input data within their uncertainty, its reconstructed spectra denote a valid hypothesis for the actual underlying spectrum. The BR method possesses an explicit default model dependence, which however can and is assessed by repeating reconstructions for different functional forms of the default model. And while the BR method is known to be susceptible to ringing artifacts, as its regulator is weakest among the reconstruction methods on the market, no signs of ringing have been observed in this study, neither in the HTL mock test nor in the reconstruction of genuine lattice data.

As a crucial limitation in the context of the current study, the BR method is only applicable to positive definite spectral functions. If effective masses show nonmonotonicity it indicates that the BR method cannot be deployed. However even if the effective masses are monotonous, positivity violation may persist, which explains why the BR method fails to converge successfully for higher temperatures on the raw Euclidean correlators. The outcome of the extraction of  $\Omega$ , based on the BR method at low temperatures such as  $T = 151$  MeV yields a real part which agrees well with the static energy from (multi-state) exponential fits, also applicable on those lattices. We find that the spectral functions show well defined Breit-Wigner like peaks, which get exponentially cut off close to the origin, similar to what is seen in HTL perturbation theory at much higher temperatures. Comparing the BR result to the Padé method we find that the Padé method incorrectly assigns too much weight to the low frequency regime and at the same time produces a less and less well-defined peak, which is consistently located at a higher position than the BR peak. Agreement between the BR method and the effective masses and the tension with the Padé method starting around  $r = 0.5$  fm seem to

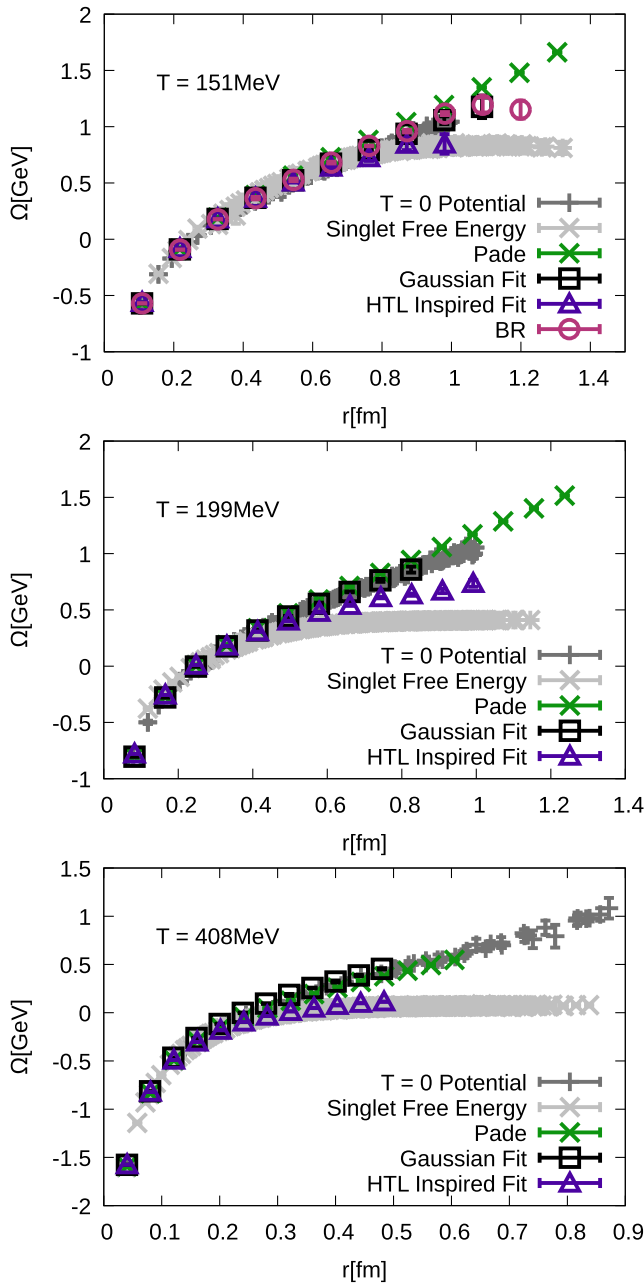


FIG. 26. Comparison of  $\Omega$  as a function of separation distance for three different temperatures 151, 199 and 408 MeV obtained from different methods discussed in the text. We have also shown the  $T = 0$  potential (dark grey) for all temperatures and the free energy (light grey) for high temperature (408 MeV).

indicate that the Padé method tends to overestimate the values of  $\Omega$  when applied to our lattice data.

The comparison of different methods of the spectral reconstruction in terms of the peak position,  $\Omega$  of the dominant peak and its width,  $\Gamma$  is summarized in Figs. 26 and 27, respectively for three temperatures,  $T = 151$  MeV (just below the chiral crossover),  $T = 199$  MeV (the typical temperature most relevant for the RHIC), and  $T = 408$  MeV deep in the QGP. The present study sheds

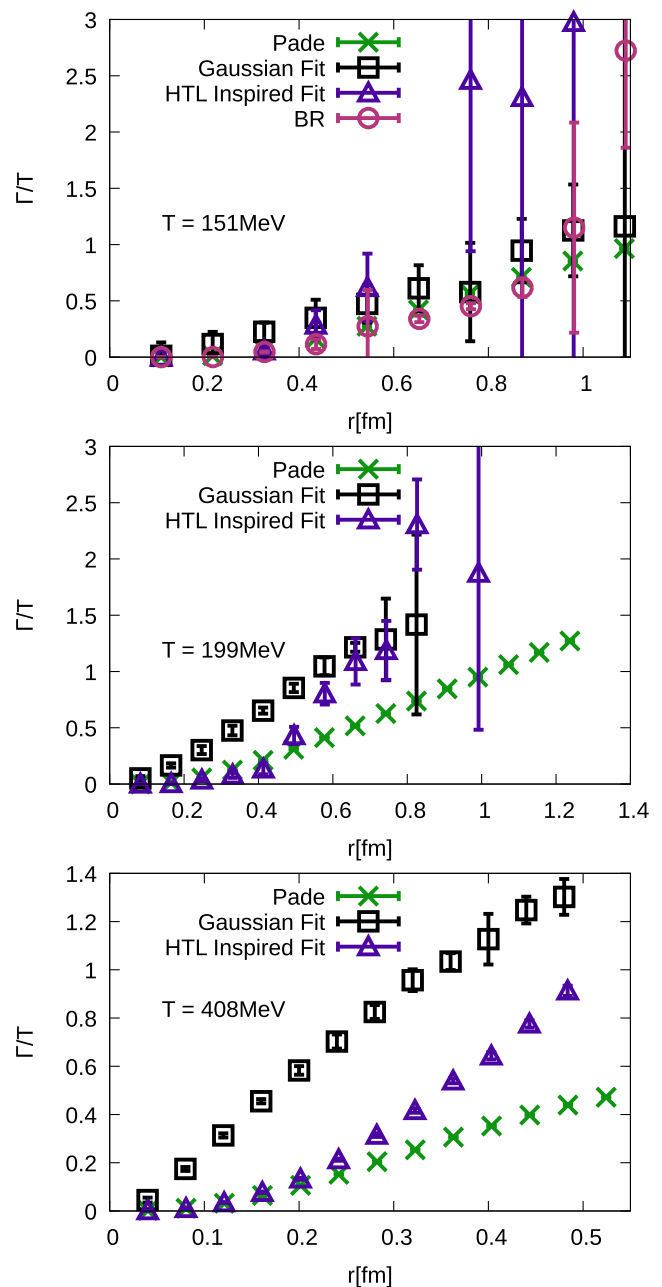


FIG. 27. Comparison of  $\Gamma/T$  as a function of separation distance for three different temperatures 151, 199 and 408 MeV obtained from different methods discussed in the text.

new light on the extraction of  $\Omega$  and  $\Gamma$ . While different methods often lead to quantitatively different results some general features are the same. The width  $\Gamma$  is significant compared to the temperature scale and increases with distance  $r$  for all temperatures. In fact, for the lowest temperature all methods give consistent results for  $\Gamma$ . For temperatures  $150 \text{ MeV} < T < 200 \text{ MeV}$ , the Gaussian fits and HTL fits lead to similar widths for large  $r$ , while at small  $r$  the HTL fit gives a smaller width. The Padé method always gives a smaller  $\Gamma$  than the Gaussian and HTL fits at large  $r$ , but agrees with the HTL result at small

$r$ , cf. Fig. 27. The  $r$  dependence of the peak position turns out to be similar for the Gaussian fits and the Padé method, indicating an apparent absence of the screening effects. Furthermore in the temperature range  $150 \text{ MeV} < T < 200 \text{ MeV}$  and at intermediate distances, all the explored methods give a peak position that is slightly larger than the singlet free energy; see Fig. 26. For these temperatures, which are the most relevant ones for the RHIC, the spread of the results is not too large in order to have an impact on the phenomenological studies. At higher temperatures, which are of interest for quarkonium phenomenology in heavy ion collisions at the LHC our results are inconclusive at present, and lattice calculations with larger  $N_\tau$  and smaller statistical errors are needed. Increasing the temporal extent of the lattice will be possible in the coming years. At the same time accumulation of statistics at  $T = 0$  will also enable a high precision subtraction, which in turn will enable us to use the BR method above the crossover temperature.

All data from our calculations, presented in the figures of this paper, can be found in [67].

### ACKNOWLEDGMENTS

This material is based upon work supported by the U.S. Department of Energy, Office of Science, Office of Nuclear Physics through Contract No. DE-SC0012704, and the Scientific Discovery through Advanced Computing (SciDAC) award Computing the Properties of Matter with Leadership Computing Resources. R. L., G. P. and A. R. acknowledge funding by the Research Council of Norway under the FRIPRO Young Research Talent Grant No. 286883. J. H. W.'s research was funded by the Deutsche Forschungsgemeinschaft (DFG, German Research Foundation)—Projektnummer 417533893/GRK2575 “Rethinking Quantum Field Theory.” D. B. and O. K. acknowledge support by the Deutsche Forschungsgemeinschaft (DFG, German Research Foundation) through the CRC-TR 211 “Strong-interaction matter under extreme conditions,” Project No. 315477589-TRR 211. This research used awards of computer time provided by: the INCITE (The Innovative and Novel Computational Impact on Theory and Experiment) and ALCC (ASCR Leadership Computing Challenge) programs at Oak Ridge Leadership Computing Facility, a DOE Office of Science User Facility operated under Contract No. DE-AC05-00OR22725; the National Energy Research Scientific Computing Center (NERSC), a U.S. Department of Energy Office of Science User Facility located at Lawrence Berkeley National Laboratory, operated under Contract No. DE-AC02-05CH11231; the PRACE (Partnership for advanced computing in Europe) award on JUWELS (Jülich Wizard for European Leadership Science) at GCS@FZJ (Gauss Centre for Supercomputing@Forschungszentrum Juelich),

Germany; the facilities of the USQCD (U.S. Lattice Quantum Chromodynamics) Collaboration, which are funded by the Office of Science of the U.S. Department of Energy; and UNINETT Sigma2, the National Infrastructure for High Performance Computing and Data Storage in Norway under Project No. NN9578K-QCDrtX “Real-time dynamics of nuclear matter under extreme conditions.” The computations in this work were performed using the SIMULATeQCD suite [68,69].

### APPENDIX A: THE SPECTRAL DECOMPOSITION OF STATIC $Q\bar{Q}$ CORRELATORS

In this Appendix we discuss the general features of the spectral decomposition of the static meson correlation function. Let  $O_r = \bar{Q}(x)U(\mathbf{x} - \mathbf{y})Q(y)$  be a static meson operator with  $r = |\mathbf{x} - \mathbf{y}|$ . The gauge connection  $U(\mathbf{x} - \mathbf{y})$  runs along the straight line connecting the spatial points  $\mathbf{x}$  and  $\mathbf{y}$  and may be constructed from smeared links on the lattice. More complicated paths are also possible. In Coulomb gauge we set  $U(\mathbf{x} - \mathbf{y}) = 1$ . The static meson correlation function at nonzero temperature is defined as

$$\begin{aligned} W(r, \tau, T) &= \langle O_r(\tau) O_r(0) \rangle \\ &= \frac{1}{Z(T)} \text{Tr}[O_r(0) e^{-\tau H} O_r(0) e^{-(\beta-\tau)H}], \\ \beta &= 1/T, \quad Z(T) = \sum_n e^{-\beta E_n}. \end{aligned} \quad (\text{A1})$$

Using the energy eigenstates to evaluate the trace in the above expression and inserting a complete set of energy eigenstates between the operators  $O_r$  the spectral decomposition of the static meson correlation function can be written as

$$W(r, \tau, T) = \frac{1}{Z(T)} \sum_{n, n'} e^{-(\beta-\tau)E_n} e^{-E_n' \tau} |\langle n | O_r(0) | n' \rangle|^2, \quad (\text{A2})$$

where  $|n\rangle$  are states without the static  $Q\bar{Q}$  pair and  $|n'\rangle$  are the states that also contain the static  $Q\bar{Q}$  pair at distance  $r$ . Since static quarks are not part of the thermal system in the evaluation of the trace we only take into account the states  $|n\rangle$ . Hereafter, we introduce  $C_{nm}^r = |\langle n | O_r | m' \rangle|^2$ . Let us take into account the few lowest terms in the spectral decomposition,  $n = 0, 1, 2$  and  $n = 0', 1', 2'$ :

$$\begin{aligned} Z(T)W(r, \tau, T) &= e^{-(\beta-\tau)E_0} e^{-E_{0'}(r)\tau} C_{00} \\ &+ e^{-(\beta-\tau)E_0} e^{-E_{1'}(r)\tau} C_{01}^r \\ &+ e^{-(\beta-\tau)E_1} e^{-E_{0'}(r)\tau} C_{10}^r \\ &+ e^{-(\beta-\tau)E_1} e^{-E_{1'}(r)\tau} C_{11}^r \\ &+ e^{-(\beta-\tau)E_0} e^{-E_{2'}(r)\tau} C_{02}^r \\ &+ e^{-(\beta-\tau)E_2} e^{-E_{0'}(r)\tau} C_{20}^r \\ &+ e^{-(\beta-\tau)E_2} e^{-E_{2'}(r)\tau} C_{22}^r. \end{aligned} \quad (\text{A3})$$

Now we assume that the energy of the vacuum is zero, while the energy of the vacuum state plus a static  $Q\bar{Q}$  is the static  $Q\bar{Q}$  energy:  $E_0 = 0$  and  $E_{Q\bar{Q}}(r) = V(r)$ . We ignore the contribution of hybrid potentials for now. For the energy of the states with a  $Q\bar{Q}$  pair plus a hadronic state we write

$$E_{n'}(r) = V(r) + E_n + \Delta E_n(r), \quad (\text{A4})$$

where  $\Delta E_n(r)$  is the interaction energy of the  $Q\bar{Q}$  pair with hadron state  $n$ , and it could be either positive or negative. For small  $r$  we expect  $\Delta E_n(r) \ll E_n$  because hadrons do not interact significantly with a tiny color singlet dipole. Now let us assume that  $|1\rangle$  has nonvacuum quantum number, i.e.,  $C_{01}^r = C_{10}^r = 0$  and state  $|2\rangle$  has vacuum quantum number, i.e.,  $C_{20}^r \neq 0$  and  $C_{20}^r \neq 0$ . Then we also have  $C_{21}^r = C_{12}^r = 0$  and the corresponding terms have been already omitted in Eq. (A3). Note that the matrix elements  $C_{02}^r$  and  $C_{20}^r$  could be small since the operator  $O_r$  is optimized to create a single static meson state, while  $|2'\rangle$  is an extended state of a static meson and a multi-hadron state with vacuum quantum numbers. Now we can write

$$\begin{aligned} Z(T)W(r, \tau, T) &= C_{00}e^{-V(r)\tau} + C_{11}e^{-\beta E_1}e^{-(V(r)+\Delta E_1(r))\tau} \\ &\quad + C_{22}e^{-\beta E_2}e^{-(V(r)+\Delta E_2(r))\tau} \\ &\quad \times C_{02}e^{-(V(r)+E_2+\Delta E_2(r))\tau} \\ &\quad + C_{20}e^{-(\beta-\tau)E_2}e^{-V(r)\tau}. \end{aligned} \quad (\text{A5})$$

The first term is the contribution of the vacuum  $Q\bar{Q}$  energy. The second and third terms are due to thermal effects, and they correspond to a broadening of the spectral function and vanish in the zero temperature limit. The fourth term is just an excited state contribution to the correlator at  $T = 0$  corresponding to a static  $Q\bar{Q}$  pair of size  $r$  and a hadron state with vacuum quantum numbers, e.g., isospin zero  $\pi\pi$  states. The last term is Boltzmann suppressed for all  $\tau$ , except for  $\tau$  very close to  $\beta$ . This is the term that causes a rapid decrease of effective masses when  $\tau \sim \beta$ . The spectral function corresponding to the above correlator can be written as

$$\rho_r(\omega, T) = \rho_r^{\text{med}}(\omega, T) + \rho_r^{\text{high}}(\omega, T) + \rho_r^{\text{tail}}(\omega, T), \quad (\text{A6})$$

$$\begin{aligned} \rho_r^{\text{med}}(\omega, T) &= \frac{1}{Z(T)} [C_{00}^r \delta(\omega - V(r)) \\ &\quad + C_{11}^r e^{-\beta E_1} \delta(\omega - V(r) - \Delta E_1(r)) \\ &\quad + C_{22}^r e^{-\beta E_2} \delta(\omega - V(r) - \Delta E_2(r))], \end{aligned} \quad (\text{A7})$$

$$\rho_r^{\text{high}}(\omega, T) = \frac{1}{Z(T)} C_{02}^r \delta(\omega - V(r) - \Delta E_2(r) - E_2), \quad (\text{A8})$$

$$\rho_r^{\text{tail}}(\omega, T) = \frac{1}{Z(T)} C_{20}^r e^{-\beta E_2} \delta(\omega - V(r) + E_2). \quad (\text{A9})$$

We see that  $\rho_r^{\text{med}}$  is a discrete version of a narrow broadened peak, while  $\rho_r^{\text{tail}}$  can have support for  $\omega$  well below the ground state peak. Note that the above considerations are valid not only for static meson correlators but also for nonrelativistic meson correlators, e.g., extended bottomonium correlators in NRQCD considered in Refs. [13,49,50].

It is straightforward to generalize the above spectral function to include all states. First, we note that  $E_{Q\bar{Q}}$  does not only correspond to the ground state  $Q\bar{Q}$  energy but also to hybrid potentials as well as static-light mesons. We denote these additional states by  $V_\alpha(r)$ ,  $\alpha \geq 1$ . If we use index  $k$  for all hadron states with vacuum quantum number (e.g., isospin zero two pion states) for the spectral function we can write

$$\rho_r(\omega, T) = \rho_r^{\text{med}}(\omega, T) + \rho_r^{\text{high}}(\omega, T) + \rho_r^{\text{tail}}(\omega, T), \quad (\text{A10})$$

$$\begin{aligned} \rho_r^{\text{med}}(\omega, T) &= \frac{1}{Z(T)} [C_{00}^r \delta(\omega - V(r)) \\ &\quad + \sum_n C_{nn}^r e^{-\beta E_n} \delta(\omega - V(r) - \Delta E_n(r))], \end{aligned} \quad (\text{A11})$$

$$\begin{aligned} \rho_r^{\text{high}}(\omega, T) &= \frac{1}{Z(T)} \left[ \sum_k C_{0k}^r \delta(\omega - V(r) - \Delta E_k(r) - E_k) \right. \\ &\quad + \sum_\alpha C_{00}^{r\alpha} \delta(\omega - V_\alpha(r)) \\ &\quad \left. + \sum_{n,\alpha} C_{nn}^{r\alpha} e^{-\beta E_n} \delta(\omega - V_\alpha(r) - \Delta E_n(r)) \right], \end{aligned} \quad (\text{A12})$$

$$\begin{aligned} \rho_r^{\text{tail}}(\omega, T) &= \frac{1}{Z(T)} \left[ \sum_k C_{k0}^r e^{-\beta E_k} \delta(\omega - V(r) + E_k) \right. \\ &\quad + \sum_\alpha \sum_k C_{k0}^{r\alpha} e^{-\beta E_k} \delta(\omega - V_\alpha(r) + E_k) \\ &\quad + \sum_{n,m \neq 0} C_{nm}^r e^{-\beta E_n} \delta(\omega - V(r) - \Delta E_m(r) - E_m + E_n) \\ &\quad \left. + \sum_\alpha \sum_{n,m \neq 0} C_{nm}^{r\alpha} e^{-\beta E_n} \delta(\omega - V_\alpha(r) \right. \\ &\quad \left. - \Delta E_m(r) - E_m + E_n) \right]. \end{aligned} \quad (\text{A13})$$

Since  $E_k$  can be very large the  $\rho_r^{\text{tail}}(\omega, T)$  can be nonzero at very small  $\omega$ . We see that the spectral function of the static  $Q\bar{Q}$  pair has three contributions: a dominant peak that is broadened at nonzero temperature, a high  $\omega$  part reflecting the excited state contributions and a low  $\omega$  tail that mostly contributes at  $\tau = \beta$ . This is exactly what we see in our lattice results.

TABLE I. Parameters of the calculations on zero temperature lattices for  $m_l = m_s/20$  (upper part) and  $m_l = m_s/5$  (lower part).

$m_l = m_s/20$						
$\beta$	a (fm)	$N_\sigma, N_\tau$	$am_s$	$m_\pi L$	#TUs	Ref.
6.740	0.109	$48^4$	0.0476	4.2	1350	[38]
6.800	0.103	$32^4$	0.0448	2.7	5650	[38]
6.880	0.095	$48^4$	0.0412	3.7	1400	[38]
6.950	0.089	$32^4$	0.0386	2.3	10830	[38]
7.030	0.083	$48^4$	0.0356	3.2	1355	[38]
7.150	0.074	$64^3 \times 48$	0.0320	2.9	1458	[38]
7.280	0.066	$64^3 \times 48$	0.0284	2.5	1734	[38]
7.373	0.060	$64^3 \times 48$	0.0250	2.3	4623	[40]
7.596	0.049	$64^4$	0.0202	2.6	4757	[40]
7.825	0.040	$64^4$	0.0164	2.0	4768	[40]
$m_l = m_s/5$						
$\beta$	a [fm]	$N_\sigma, N_\tau$	$am_s$	$m_\pi L$	#TUs	Ref.
8.000	0.035	$64^4$	0.01299	3.6	4616	[42]
8.200	0.029	$64^4$	0.01071	3.1	4616	[42]
8.400	0.025	$64^4$	0.00887	2.6	4616	[42]

## APPENDIX B: PARAMETERS OF THE CALCULATIONS, QUARK MASS AND CUTOFF EFFECTS

In this Appendix we summarize the parameters used in our lattice calculations, including the bare gauge coupling  $\beta = 10/g_0^2$ , the quark masses, the corresponding temperature values, as well as the corresponding statistics in terms of molecular dynamic time units (TUs). Measurements of the Wilson loops and Wilson line correlators have been performed every 10 TUs. We also discuss some systematic errors in our calculations such as quark mass effects and cutoff effects.

The parameters and statistics for the zero temperature lattices are summarized in Table I. The parameters for  $N_\tau = 16, 12$  and  $10$  lattice are shown in Tables II–IV, respectively.

As one can see from the tables for  $N_\tau = 10$  and  $N_\tau = 12$  lattices we have calculations at the same values of  $\beta = 8.0, 8.2$  and  $8.4$  but with different quark masses. In Fig. 28 we show the comparison of the effective masses calculated at different sea quark masses for  $N_\tau = 10$  and  $12$ . We see from the figures that there is no statistically significant difference between the calculations performed for  $m_l = m_s/5$  and  $m_s/20$ . Thus we conclude that the quark mass effects are small for temperatures  $T > 474$  MeV.

 TABLE II. Parameters of the  $64^3 \times 16$  calculations for the two different light quark masses. The lower part of the table corresponds to  $m_l = m_s/5$ , while the upper part corresponds to  $m_l = m_s/20$ .

$m_l = m_s/20$			
$\beta$	$am_s$	T (MeV)	#TUs
7.825	0.00164	306	67960
8.570	0.008376	577	10400
8.710	0.007394	650	10190
8.850	0.006528	731	4480
9.060	0.004834	872	41870
9.230	0.004148	1005	3610
9.360	0.003691	1121	3530
9.490	0.003285	1250	6790
9.670	0.002798	1454	42060
$m_l = m_s/5$			
$\beta$	$am_s$	T (MeV)	#TUs
8.000	0.001299	356	11460
8.200	0.001071	422	10660
8.400	0.000887	500	64370

We study cutoff effects in terms of the second cumulant,  $m_2$ . In Fig. 29 we show the  $N_\tau$  dependence of the square root of negative  $m_2$  as function of  $\tau T$  for temperatures which are very close. We do not see a statistically significant  $N_\tau$  dependence.

## APPENDIX C: QUALITY OF THE FITS OF THE $Q\bar{Q}$ CORRELATION FUNCTION

In this Appendix we discuss the quality of the fit of the static  $Q\bar{Q}$  correlation function in Coulomb gauge with the Gaussian form given by Eq. (12) and with the HTL inspired (Bala-Datta) form given by Eq. (21). In Fig. 30 we show the residue of the Gaussian fits in terms of the first cumulant for three representative temperatures and  $rT = 1/4, 1/2$  and  $3/4$ . As one can see from the figure the Gaussian form describes the Wilson line correlator very well in the entire  $\tau$  range, with possibly an exception of the  $\tau = a$  data point at high temperatures.

In Fig. 31 we show the residual of the fits for the Bala-Datta form for the first cumulant. For the shortest distance,  $rT = 1/4$  the fit captures the data well, except at the shortest and largest values of  $\tau$ . For larger distances this fit only works for  $\tau T$  around  $1/2$ .

TABLE III. Parameters of the calculations on  $48^3 \times 12$  lattices for  $m_l = m_s/20$  (upper part) and  $m_l = m_s/5$  (lower part).

$m_l = m_s/20$			
$\beta$	$am_s$	T (MeV)	#TUs
6.515	0.0604	122	32500
6.608	0.0542	133	19990
6.664	0.0514	141	45120
6.700	0.0496	146	15900
6.740	0.0476	151	29410
6.770	0.0460	156	15530
6.800	0.0448	160	36060
6.840	0.0430	166	17370
6.880	0.0412	173	46350
6.950	0.0386	185	50550
7.030	0.0378	199	65940
7.100	0.0332	213	9640
7.150	0.0320	223	9600
7.200	0.0296	233	4010
7.280	0.0284	251	58210
7.373	0.0250	273	85120
7.596	0.0202	334	98010
7.650	0.0202	350	3230
7.825	0.0164	408	134600
8.000	0.0140	474	3110
8.200	0.01167	562	30090
8.400	0.00975	667	29190
8.570	0.008376	770	6320
8.710	0.007394	866	6490
8.850	0.006528	974	6340
9.060	0.004834	1162	7430
9.230	0.004148	1340	7280
9.360	0.003691	1495	7910
9.490	0.003285	1667	9780
9.670	0.002798	1938	7650
$m_l = m_s/5$			
$\beta$	$am_s$	T (MeV)	#TUs
8.000	0.01299	474	71670
8.200	0.01071	563	71390
8.400	0.00887	667	71170

TABLE IV. Parameters of the calculations on  $40^3 \times 10$  lattices for  $m_l = m_s/20$  (upper part) and  $m_l = m_s/5$  (lower part).

$m_l = m_s/20$			
$\beta$	$am_s$	T (MeV)	#TUs
6.285	0.0790	116	9260
6.341	0.0740	123	39190
6.423	0.0670	133	10360
6.488	0.0620	142	102690
6.515	0.0604	146	107530
6.575	0.0564	155	106020
6.608	0.0542	160	112890
6.664	0.0514	169	155440
6.740	0.0476	181	200250
6.800	0.0448	192	279830
6.880	0.0412	208	341490
6.950	0.0386	222	243480
7.030	0.0378	239	137730
7.150	0.0320	267	145440
7.280	0.0284	301	105990
7.373	0.0250	328	50840
7.596	0.0202	400	51710
7.825	0.0164	489	54000
8.000	0.0140	569	6780
8.200	0.01167	675	27500
8.400	0.00975	800	7540
8.570	0.008376	924	3000
8.710	0.007394	1039	15320
8.850	0.006528	1169	7690
9.060	0.004834	1395	15490
9.230	0.004148	1608	7630
9.360	0.003691	1794	15800
9.490	0.003285	2000	7990
9.670	0.002798	2326	15760
$m_l = m_s/5$			
$\beta$	$am_s$	T (MeV)	#TUs
8.000	0.01299	569	82770
8.200	0.01071	675	72180
8.400	0.00887	800	72770

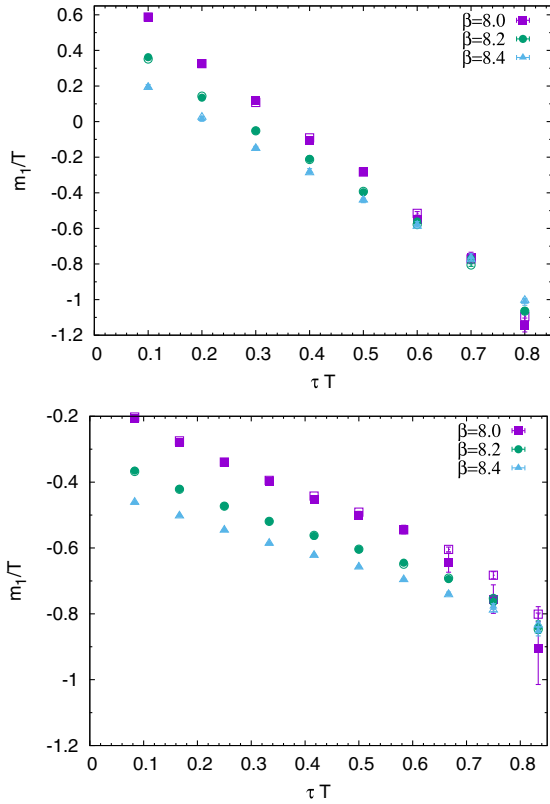


FIG. 28. The first cumulants calculated for  $N_\tau = 10$ ,  $rT = 1$  (top) and  $N_\tau = 12$ ,  $rT = 1/2$  (bottom) for  $\beta = 8.0, 8.2$  and  $8.4$  for different quark masses. The open symbols correspond to  $m_s/5$  calculations, while the filled symbols correspond to  $m_s/20$  calculations.

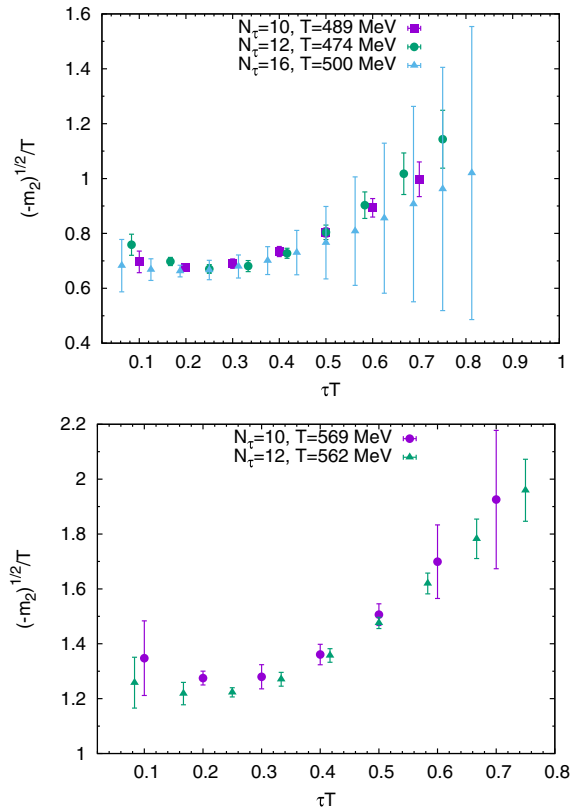


FIG. 29. The cutoff dependence of the second cumulant for temperatures around 500 MeV (top) and around 570 MeV (bottom) for distances  $rT = 1/2$  and  $rT = 1$ , respectively.

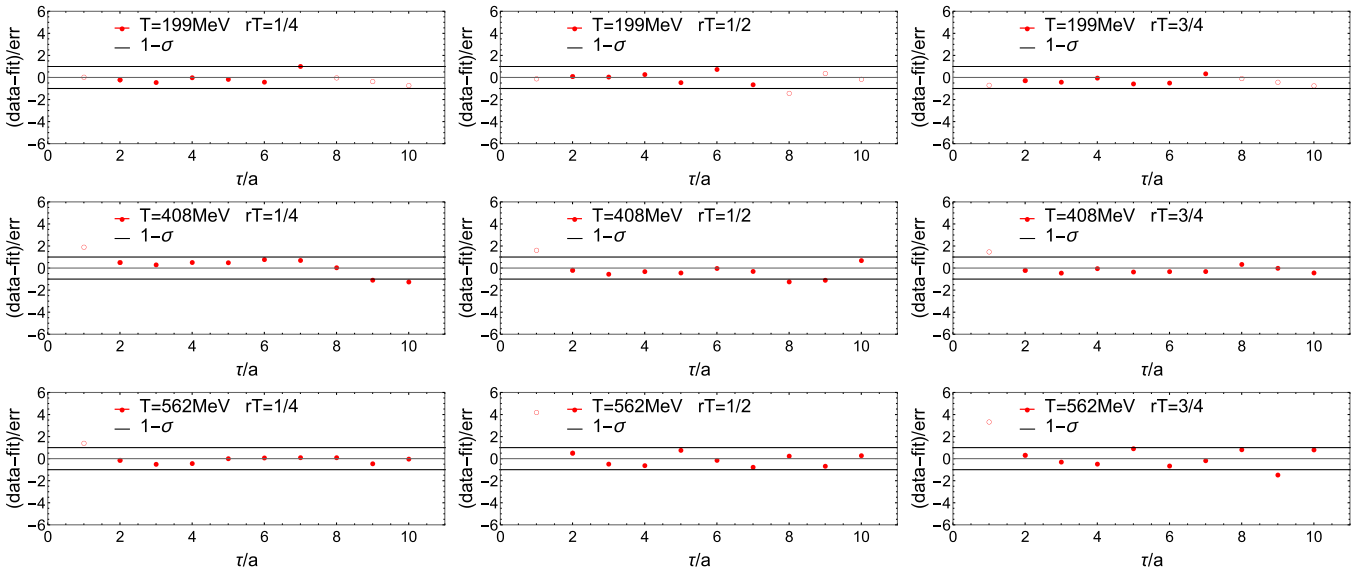


FIG. 30. The difference between the Gaussian fit and the lattice data on the first cumulant for  $N_\tau = 12$  as a function of  $\tau$  normalized by the statistical errors for  $rT = 1/4$  (left),  $rT = 1/2$  (middle) and  $rT = 3/4$  (right). The top row shows the result for  $T = 199$  MeV, the middle row shows the result for  $T = 408$  MeV, while the bottom row corresponds to  $T = 562$  MeV. The open symbols correspond to the data points not included in the fit.

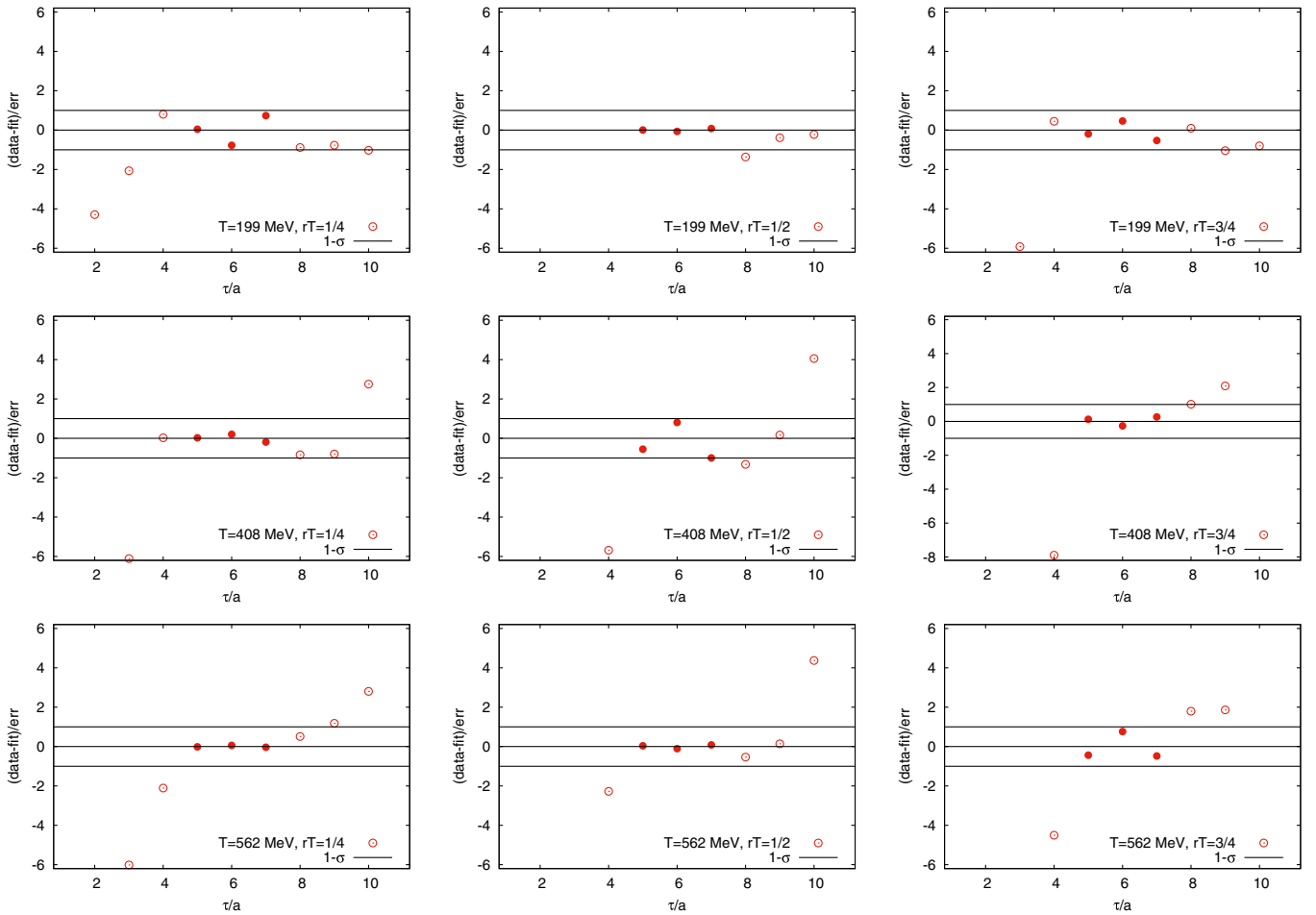


FIG. 31. The difference between the Bala-Datta fit and the lattice data on the first cumulant for  $N_\tau = 12$  as a function of  $\tau$  normalized by the statistical errors for  $rT = 1/4$  (left),  $rT = 1/2$  (middle) and  $rT = 3/4$  (right). The top row shows the result for  $T = 199$  MeV, the middle row shows the result for  $T = 408$  MeV, while the bottom row corresponds to  $T = 562$  MeV. The open symbols correspond to the data points not included in the fit.

- 
- [1] A. Rothkopf, Heavy quarkonium in extreme conditions, *Phys. Rep.* **858**, 1 (2020).
- [2] G. Aarts *et al.*, Heavy-flavor production and medium properties in high-energy nuclear collisions—What next?, *Eur. Phys. J. A* **53**, 93 (2017).
- [3] A. Mocsy, P. Petreczky, and M. Strickland, Quarkonia in the quark gluon plasma, *Int. J. Mod. Phys. A* **28**, 1340012 (2013).
- [4] A. Bazavov, P. Petreczky, and A. Velytsky, Quarkonium at finite temperature, in *Quark-Gluon Plasma 4*, edited by R. C. Hwa and X.-N. Wang (World Scientific, Singapore, 2010), pp. 61–110.
- [5] T. Matsui and H. Satz,  $J/\psi$  suppression by quark-gluon plasma formation, *Phys. Lett. B* **178**, 416 (1986).
- [6] A. Bazavov and J.H. Weber, Color screening in quantum chromodynamics, *Prog. Part. Nucl. Phys.* **116**, 103823 (2021).
- [7] A. Bazavov, N. Brambilla, P. Petreczky, A. Vairo, and J. H. Weber (TUMQCD), Color screening in  $(2 + 1)$ -flavor QCD, *Phys. Rev. D* **98**, 054511 (2018).
- [8] N. Brambilla *et al.* (Quarkonium Working Group), Heavy quarkonium physics, [arXiv:hep-ph/0412158](https://arxiv.org/abs/hep-ph/0412158).
- [9] T. Kawanai and S. Sasaki, Interquark Potential with Finite Quark Mass from Lattice QCD, *Phys. Rev. Lett.* **107**, 091601 (2011).
- [10] T. Kawanai and S. Sasaki, Charmonium potential from full lattice QCD, *Phys. Rev. D* **85**, 091503 (2012).
- [11] T. Kawanai and S. Sasaki, Heavy quarkonium potential from Bethe-Salpeter wave function on the lattice, *Phys. Rev. D* **89**, 054507 (2014).
- [12] K. Nochi, T. Kawanai, and S. Sasaki, Bethe-Salpeter wave functions of  $\eta_c(2S)$  and  $\psi(2S)$  states from full lattice QCD, *Phys. Rev. D* **94**, 114514 (2016).

- [13] R. Larsen, S. Meinel, S. Mukherjee, and P. Petreczky, Bethe-salpeter amplitudes of upsilons, *Phys. Rev. D* **102**, 114508 (2020).
- [14] W. Caswell and G. Lepage, Effective lagrangians for bound state problems in QED, QCD, and other field theories, *Phys. Lett.* **167B**, 437 (1986).
- [15] N. Brambilla, A. Pineda, J. Soto, and A. Vairo, Potential NRQCD: An effective theory for heavy quarkonium, *Nucl. Phys.* **B566**, 275 (2000).
- [16] M. Laine, O. Philipsen, P. Romatschke, and M. Tassler, Real-time static potential in hot QCD, *J. High Energy Phys.* **03** (2007) 054.
- [17] N. Brambilla, J. Ghiglieri, A. Vairo, and P. Petreczky, Static quark-antiquark pairs at finite temperature, *Phys. Rev. D* **78**, 014017 (2008).
- [18] A. Beraudo, J. P. Blaizot, and C. Ratti, Real and imaginary-time Q anti-Q correlators in a thermal medium, *Nucl. Phys.* **A806**, 312 (2008).
- [19] Y. Burnier and A. Rothkopf, Bayesian Approach to Spectral Function Reconstruction for Euclidean Quantum Field Theories, *Phys. Rev. Lett.* **111**, 182003 (2013).
- [20] A. Rothkopf, T. Hatsuda, and S. Sasaki, Complex Heavy-Quark Potential at Finite Temperature from Lattice QCD, *Phys. Rev. Lett.* **108**, 162001 (2012).
- [21] Y. Burnier and A. Rothkopf, Complex heavy-quark potential and Debye mass in a gluonic medium from lattice QCD, *Phys. Rev. D* **95**, 054511 (2017).
- [22] Y. Burnier, O. Kaczmarek, and A. Rothkopf, Static Quark-Antiquark Potential in the Quark-Gluon Plasma from Lattice QCD, *Phys. Rev. Lett.* **114**, 082001 (2015).
- [23] Y. Burnier, O. Kaczmarek, and A. Rothkopf, Quarkonium at finite temperature: Towards realistic phenomenology from first principles, *J. High Energy Phys.* **12** (2015) 101.
- [24] D. Bala and S. Datta, Nonperturbative potential for the study of quarkonia in QGP, *Phys. Rev. D* **101**, 034507 (2020).
- [25] A. Bazavov, Y. Burnier, and P. Petreczky, Lattice calculation of the heavy quark potential at non-zero temperature, *Nucl. Phys.* **A932**, 117 (2014).
- [26] P. Petreczky and J. Weber (TUMQCD Collaboration), Lattice calculations of heavy quark potential at finite temperature, *Nucl. Phys.* **A967**, 592 (2017).
- [27] N. Brambilla, M. A. Escobedo, J. Soto, and A. Vairo, Quarkonium suppression in heavy-ion collisions: an open quantum system approach, *Phys. Rev. D* **96**, 034021 (2017).
- [28] N. Brambilla, M. A. Escobedo, J. Soto, and A. Vairo, Heavy quarkonium suppression in a fireball, *Phys. Rev. D* **97**, 074009 (2018).
- [29] N. Brambilla, M. A. Escobedo, A. Vairo, and P. Vander Griend, Transport coefficients from in medium quarkonium dynamics, *Phys. Rev. D* **100**, 054025 (2019).
- [30] N. Brambilla, M. A. Escobedo, M. Strickland, A. Vairo, P. Vander Griend, and J. H. Weber, Bottomonium suppression in an open quantum system using the quantum trajectories method, *J. High Energy Phys.* **05** (2021) 136.
- [31] Y. Akamatsu, Quarkonium in quark-gluon plasma: Open quantum system approaches re-examined, *Prog. Part. Nucl. Phys.* **123**, 103932 (2022).
- [32] S. Kajimoto, Y. Akamatsu, M. Asakawa, and A. Rothkopf, Dynamical dissociation of quarkonia by wave function decoherence, *Phys. Rev. D* **97**, 014003 (2018).
- [33] T. Miura, Y. Akamatsu, M. Asakawa, and A. Rothkopf, Quantum Brownian motion of a heavy quark pair in the quark-gluon plasma, *Phys. Rev. D* **101**, 034011 (2020).
- [34] A. Rothkopf, T. Hatsuda, and S. Sasaki, Proper heavy-quark potential from a spectral decomposition of the thermal Wilson loop, Proc. Sci., LAT2009 (2009) 162 [arXiv:0910.2321], <https://pos.sissa.it/091/162>.
- [35] O. Jahn and O. Philipsen, The Polyakov loop and its relation to static quark potentials and free energies, *Phys. Rev. D* **70**, 074504 (2004).
- [36] A. Bazavov, P. Petreczky, and A. Velytsky, Static quark anti-quark pair in SU(2) gauge theory, *Phys. Rev. D* **78**, 114026 (2008).
- [37] Y. Burnier and A. Rothkopf, A hard thermal loop benchmark for the extraction of the nonperturbative  $Q\bar{Q}$  potential, *Phys. Rev. D* **87**, 114019 (2013).
- [38] A. Bazavov *et al.*, The chiral and deconfinement aspects of the QCD transition, *Phys. Rev. D* **85**, 054503 (2012).
- [39] A. Bazavov, H. T. Ding, P. Hegde, F. Karsch, C. Miao, S. Mukherjee, P. Petreczky, C. Schmidt, and A. Velytsky, Quark number susceptibilities at high temperatures, *Phys. Rev. D* **88**, 094021 (2013).
- [40] A. Bazavov *et al.* (HotQCD Collaboration), Equation of state in (2 + 1)-flavor QCD, *Phys. Rev. D* **90**, 094503 (2014).
- [41] H. T. Ding, S. Mukherjee, H. Ohno, P. Petreczky, and H. P. Schadler, Diagonal and off-diagonal quark number susceptibilities at high temperatures, *Phys. Rev. D* **92**, 074043 (2015).
- [42] A. Bazavov, P. Petreczky, and J. Weber, Equation of state in 2 + 1 flavor QCD at high temperatures, *Phys. Rev. D* **97**, 014510 (2018).
- [43] A. Bazavov, N. Brambilla, X. Garcia i Tormo, P. Petreczky, J. Soto, A. Vairo, and J. H. Weber (TUMQCD Collaboration), Determination of the QCD coupling from the static energy and the free energy, *Phys. Rev. D* **100**, 114511 (2019).
- [44] While a few ensembles actually have  $N_\tau = 2N_\sigma$ , this is irrelevant for the considerations in the following.
- [45] It is usually referred to as the potential in the lattice literature.
- [46] A. Bazavov *et al.* (MILC Collaboration), Results for light pseudoscalar mesons, Proc. Sci., LATTICE2010 (2010) 074 [arXiv:1012.0868], <https://pos.sissa.it/105/074>.
- [47] R. Sommer, A new way to set the energy scale in lattice gauge theories and its applications to the static force and alpha-s in SU(2) Yang-Mills theory, *Nucl. Phys.* **B411**, 839 (1994).
- [48] A. Bazavov, N. Brambilla, H. T. Ding, P. Petreczky, H. P. Schadler, A. Vairo, and J. H. Weber, Polyakov loop in 2 + 1 flavor QCD from low to high temperatures, *Phys. Rev. D* **93**, 114502 (2016).
- [49] R. Larsen, S. Meinel, S. Mukherjee, and P. Petreczky, Thermal broadening of bottomonia: Lattice nonrelativistic QCD with extended operators, *Phys. Rev. D* **100**, 074506 (2019).
- [50] R. Larsen, S. Meinel, S. Mukherjee, and P. Petreczky, Excited bottomonia in quark-gluon plasma from lattice QCD, *Phys. Lett. B* **800**, 135119 (2020).

- [51] C. W. Bernard, T. Burch, K. Orginos, D. Toussaint, T. A. DeGrand, C. E. DeTar, S. A. Gottlieb, U. M. Heller, J. E. Hetrick, and B. Sugar, The Static quark potential in three flavor QCD, *Phys. Rev. D* **62**, 034503 (2000).
- [52] M. Cheng *et al.*, The QCD equation of state with almost physical quark masses, *Phys. Rev. D* **77**, 014511 (2008).
- [53] P. Petreczky and J. H. Weber, Strong coupling constant from moments of quarkonium correlators revisited, *Eur. Phys. J. C* **82**, 64 (2022).
- [54] S. Shi, K. Zhou, J. Zhao, S. Mukherjee, and P. Zhuang, Heavy quark potential in QGP: DNN meets LQCD, *Phys. Rev. D* **105**, 014017 (2022).
- [55] Y. Burnier, M. Laine, and M. Vepsalainen, Heavy quarkonium in any channel in resummed hot QCD, *J. High Energy Phys.* **01** (2008) 043.
- [56] D. Bala and S. Datta, Interaction potential between heavy  $Q\bar{Q}$  in a color octet configuration in the QGP from a study of hybrid Wilson loops, *Phys. Rev. D* **103**, 014512 (2021).
- [57] R.-A. Tripolt, P. Gubler, M. Ulybyshev, and L. Von Smekal, Numerical analytic continuation of Euclidean data, *Comput. Phys. Commun.* **237**, 129 (2019).
- [58] A. K. Cyrol, J. M. Pawłowski, A. Rothkopf, and N. Wink, Reconstructing the gluon, *SciPost Phys.* **5**, 065 (2018).
- [59] Y. Burnier, M. Laine, and L. Mether, A test on analytic continuation of thermal imaginary-time data, *Eur. Phys. J. C* **71**, 1619 (2011).
- [60] L. Schlessinger, Use of analyticity in the calculation of nonrelativistic scattering amplitudes, *Phys. Rev.* **167**, 1411 (1968).
- [61] S. Necco and R. Sommer, The  $N(f) = 0$  heavy quark potential from short to intermediate distances, *Nucl. Phys.* **B622**, 328 (2002).
- [62] R.-A. Tripolt, I. Haritan, J. Wambach, and N. Moiseyev, Threshold energies and poles for hadron physical problems by a model-independent universal algorithm, *Phys. Lett. B* **774**, 411 (2017).
- [63] Y. Burnier and A. Rothkopf, Disentangling the timescales behind the non-perturbative heavy quark potential, *Phys. Rev. D* **86**, 051503 (2012).
- [64] P. Petreczky, A. Rothkopf, and J. Weber, Realistic in-medium heavy-quark potential from high statistics lattice QCD simulations, *Nucl. Phys.* **A982**, 735 (2019).
- [65] M. Asakawa, T. Hatsuda, and Y. Nakahara, Maximum entropy analysis of the spectral functions in lattice QCD, *Prog. Part. Nucl. Phys.* **46**, 459 (2001).
- [66] C. S. Fischer, J. M. Pawłowski, A. Rothkopf, and C. A. Welzbacher, Bayesian analysis of quark spectral properties from the Dyson-Schwinger equation, *Phys. Rev. D* **98**, 014009 (2018).
- [67] D. Bala, O. Kaczmarek, R. Larsen, S. Mukherjee, G. Parkar, P. Petreczky, A. Rothkopf, and J. H. Weber, Data publication: Static quark anti-quark interactions at non-zero temperature from lattice QCD, Bielefeld University, 2022, [10.4119/unibi/2961713](https://doi.org/10.4119/unibi/2961713).
- [68] L. Mazur, Topological aspects in lattice QCD, Ph.D. thesis, Bielefeld University, 2021, [10.4119/unibi/2956493](https://doi.org/10.4119/unibi/2956493).
- [69] L. Altenkort, D. Bollweg, D. A. Clarke, O. Kaczmarek, L. Mazur, C. Schmidt, P. Scior, and H.-T. Shu, HotQCD on multi-GPU systems, [arXiv:2111.10354](https://arxiv.org/abs/2111.10354).